AGU PUBLICATIONS

Geochemistry, Geophysics, Geosystems

RESEARCH ARTICLE
10.1002/2014GC005459

Sulfur isotope evolution in sulfide ores from Western Alps: Assessing the influence of subduction-related metamorphism

Fabio Giacometti[1], Katy A. Evans[2], Gisella Rebay[1], John Cliff[3], Andrew G. Tomkins[4], Piergiorgio Rossetti[5], Gloria Vaggelli[6], and David T. Adams[7]

[1]Dipartimento di Scienze della Terra e dell'Ambiente, Università degli Studi di Pavia, Pavia, Italy, [2]School of Applied Geology, Curtin University, Perth, Western Australia, Australia, [3]Centre for Microscopy, Characterization and Analysis, University of Western Australia, Perth, Western Australia, Australia, [4]School of Geosciences, Monash University, Melbourne, Victoria, Australia, [5]Dipartimento di Scienze della Terra, Università di Torino, Torino, Italy, [6]CNR-Istituto di Geoscienze e Georisorse, Torino, Italy, [7]ARC Centre of Excellence for Core to Crust Fluid Systems and GEMOC National Key Centre, Department of Earth and Planetary Sciences, Macquarie University, Sydney, New South Wales, Australia

Key Points:
- Fluid circulation and deformation favor the reequilibration of sulfur isotopes
- Negligible fluid circulation and sulfur release occurred during metamorphism
- The mobilization of metals during subduction is minimal in these study cases

Supporting Information:
- Readme
- Supporting Information

Correspondence to:
F. Giacometti,
fabio.giacometti@unipv.it

Citation:
Giacometti, F., K. A. Evans, G. Rebay, J. Cliff, A. G. Tomkins, P. Rossetti, G. Vaggelli, and D. T. Adams (2014), Sulfur isotope evolution in sulfide ores from Western Alps: Assessing the influence of subduction-related metamorphism, *Geochem. Geophys. Geosyst.*, *15*, 3808–3829, doi:10.1002/2014GC005459.

Received 17 JUN 2014
Accepted 28 AUG 2014
Accepted article online 9 SEP 2014
Published online 18 OCT 2014

Abstract Sulfides entering subduction zones can play an important role in the release of sulfur and metals to the mantle wedge and contribute to the formation of volcanic arc-associated ores. Fractionation of stable sulfur isotopes recorded by sulfides during metamorphism can provide evidence of fluid-rock interactions during metamorphism and give insights on sulfur mobilization. A detailed microtextural and geochemical study was performed on mineralized samples from two ocean floor-related sulfide deposits (Servette and Beth-Ghinivert) in high-pressure units of the Italian Western Alps, which underwent different metamorphic evolutions. The combination of microtextural investigations with $\delta^{34}S$ values from in situ ion probe analyses within individual pyrite and chalcopyrite grains allowed evaluation of the effectiveness of metamorphism in modifying the isotopic record and mobilizing sulfur and metals and have insights on fluid circulation within the slab. Textures and isotopic compositions inherited from the protolith are recorded at Beth-Ghinivert, where limited metamorphic recrystallization is attributed to limited interaction with metamorphic fluids. Isotopic modification by metamorphic processes occurred only at the submillimeter scale at Servette, where local interactions with infiltrating hydrothermal fluid are recorded by metamorphic grains. Notwithstanding the differences recorded by the two deposits, neither underwent intensive isotopic reequilibration or records evidence of intense fluid-rock interaction and S mobilization during metamorphism. Therefore, subducted sulfide deposits dominated by pyrite and chalcopyrite are unlikely to release significant quantities of sulfur to the mantle wedge and to arc magmatism sources at metamorphic grades below the lower eclogite facies.

1. Introduction

Subduction zones play an important role in global element geochemical cycles. Subduction, magmatism, and hydrothermal circulation through ocean crust are the processes that control the exchange of major, minor, and trace elements between the Earth's interior and the atmosphere [e.g., *Scambelluri et al.*, 1997; *Hoffman*, 1998; *Plank and Langmuir*, 1998; *Kerrick and Connolly*, 2001; *Manning*, 2004; *Bebout*, 2007]. Subduction of hydrated ocean lithosphere drives metamorphic devolatilization reactions that produce H_2O and CO_2-bearing fluids, which migrate to the slab-mantle interface [*Kerrick and Connolly*, 2001]. H_2O-rich fluids may then transfer leached chemical species from the slab into the mantle wedge. Water release from the slab is considered necessary for hydration of the originally anhydrous mantle wedge and facilitates partial melting [e.g., *Schmidt and Poli*, 1998; *Manning*, 2004; *Scambelluri et al.*, 2004].

Although H_2O and CO_2 are the dominant end-members present in slab-derived fluids, S and other minor components such as Cl and F play an important role in subduction zone processes. Each of these elements can form aqueous complexes with various metals, mobilizing normally nonreactive elements that can be of economic interest [e.g., *Alt et al.*, 1993; *Alirezaei and Cameron*, 2001, and references therein; *Cooke and Hollings*, 2005; *Manning*, 2011; *Spandler and Pirard*, 2013]. S-bearing fluids may leach and mobilize ore metals from sulfide deposits undergoing subduction (i.e., volcanogenic massive sulfide deposits, VMS). Such slab-derived fluids can introduce sulfur and ore metals into the overlying mantle wedge and contribute to the

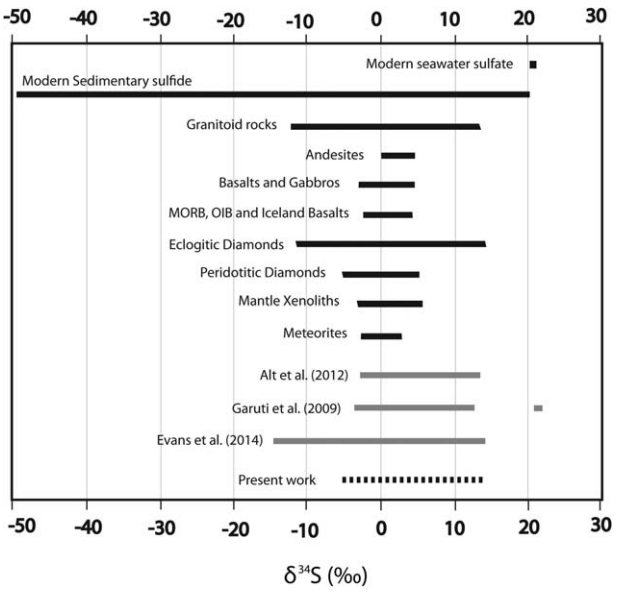

Figure 1. δ^{34}S variability for sulfides from different terrestrial reservoirs, meteorites, and for modern seawater sulfate. Data represented with black solid lines were taken from *Ohmoto and Rye* [1979], *Seal* [2006], and *Marini et al.* [2011]. Gray lines for ophiolites from the Apennines and Ligurian Alps [*Garuti et al.*, 2009; *Alt et al.*, 2012] and from the Western Alps and New Caledonia [*Evans et al.*, 2014]. Black dotted lines refer to the present work.

formation of volcanic arc-associated ores, such as porphyry copper deposits [e.g., *Sillitoe*, 1972a, 1972b; *Sawkins*, 1990; *Evans and Tomkins*, 2011; *Hannington*, 2013; *Evans et al.*, 2014, and references therein]. Evidence that slab-derived fluids contaminate the overlying mantle wedge and arc magmatism sources is provided by S isotopes. High δ^{34}S values extracted from sulfide inclusions in eclogite-facies diamonds [*Chaussidon et al.*, 1987] and from bulk arc glasses and basalts [e.g., *Alt et al.*, 1993; *de Hoog et al.*, 2001] have previously been interpreted as evidence that slab-derived ^{34}S-enriched fluids were added to the mantle and to the magmatic source of arc volcanism.

Moreover, slab-derived sulfur may contribute to the redox budget of the mantle wedge and possibly influence the redox state of arc magmas [*Evans*, 2006, 2012; *Kelley and Cottrell*, 2009; *Evans and Tomkins*, 2011]. Sulfur can occur in different oxidation states (valence -2, -1, 0, $+4$, or $+6$) and may be released by processes associated with subduction, possibly after a change in valence due to oxidation-reduction reactions. Since one mole of S^{6+} has the potential to oxidize eight moles of Fe^{2+} to Fe^{3+} when S^{6+} is reduced to S^{2-} [*Kelley and Cottrell*, 2009], S may be a significant oxidant of subarc mantle.

Sulfide deposits are widespread in the Italian Western Alps and Northern Apennine ophiolites. These ophiolites are portions of the oceanic lithosphere of the Piedmont ocean of Jurassic to Late Cretaceous age [e.g., *Lemoine et al.*, 1987, and references therein; *Polino et al.*, 1990; *Rubatto et al.*, 1998; *Castellarin*, 2001; *Dal Piaz et al.*, 2003; *Carminati and Doglioni*, 2012]. Ophiolites from the Western Alps are pervasively affected by subduction-related metamorphism and deformation.

In this paper, we investigate two ocean floor-related sulfide deposits from the Western Alps: the blueschists-facies Beth-Ghinivert (Chisone Valley) and the eclogite-facies Servette (St. Marcel Valley) deposits. These deposits underwent polyphase metamorphism from high pressure-low temperature (HP-LT) to greenschist facies during the Alpine Orogeny.

A combination of textural observations, maps of trace element relative abundances, and in situ analyses of δ^{34}S within individual pyrite and chalcopyrite grains (SIMS analyses) allows evaluation of the extent of recrystallization and fluid-rock interaction during metamorphism. The comparison between the two deposits allows assessment of the relative roles of temperature, infiltration of external fluids, and deformation on the metamorphic evolution of sulfide mineralization. Results are used to constrain the nature of metamorphic fluids in the subduction zones and the role of high-pressure metamorphism in the mobilization of sulfur and metals of economic interest.

2. Overview of Sulfur Isotopes

2.1. Ocean Floor-Related Sulfide Deposits

Several studies indicate that δ^{34}S values in sulfides found in unaltered mid-ocean ridge gabbros and basalts ($-0.3 \pm 2.3‰$ in MORB basalt) approach the composition of sulfides in meteorites (Figure 1) [*Ohmoto and Rye*, 1979; *Seal*, 2006; *Marini et al.*, 2011]. Sulfides from ocean-floor hydrothermal and sedimentary deposits, on the other hand, show heterogeneous δ^{34}S values (ranging from -50 to $40‰$), at all scales from deposit

to single crystal, due to organic and inorganic processes of isotopic fractionation (Figure 1) [e.g., *Sangster*, 1971; *Janecky and Seyfried*, 1984; *Alt and Chaussidon*, 1989; *Cook and Hoefs*, 1997; *Velasco et al*., 1998; *Garuti et al*., 2009].

Sulfur isotope fractionation is controlled by redox conditions, temperature, pH, and kinetic factors [*Bachinski*, 1969; *Ohmoto and Rye*, 1979; *Ohmoto and Lasaga*, 1982; *Ohmoto and Goldhaber*, 1997; *Seal*, 2006]. Therefore, variation of δ^{34}S at deposit and microscale can be due to a combination of processes, such as mixing of different S sources (i.e., S-bearing fluids separated from magmas, sulfides leached from host magmatic or sedimentary rock, organically and/or inorganically reduced seawater sulfate), cooling of hydrothermal fluids, kinetic effects during precipitation of S-bearing minerals in open and closed systems, and variations of pH and Eh conditions [*Ohmoto and Rye*, 1979; *Puchelt and Hubberten*, 1980; *Alt and Chaussidon*, 1989; *Strauss and Schieber*, 1990; *Calvert et al*., 1996; *Seal*, 2006].

2.2. Insights From Obducted and Subducted Ophiolites of the Piedmont Ocean

Deformation, recrystallization, dissolution-precipitation, fluid-rock interaction, diffusion, and isotope-exchange reactions occurring during metamorphism are likely to cause progressive rehomogenization of isotopic compositions within sulfides at different scales, even though primary isotope distribution patterns have been in part preserved in many metamorphosed deposits [e.g., *Sangster*, 1971; *Cook and Hoefs*, 1997; *Alirezaei and Cameron*, 2001; *Wagner and Boyce*, 2006; *Evans et al*., 2014].

Sulfide deposits from the Apennines, which did not undergo subduction, are likely to record isotopic characteristics similar to those that may have existed in sulfide deposits in the Western Alps before they underwent HP metamorphism. Bulk mineral analyses of S isotopes have been performed on a number of sulfide deposits hosted by Northern Apennine ophiolites [*Garuti et al*., 2009]. This bulk mineral approach does not allow an evaluation of intracrystalline heterogeneities. Nevertheless, the authors found that δ^{34}S was heterogeneous at sample scale in all the different settings and sampling zones investigated: δ^{34}S values in sulfide ores deposited at the ocean floor range from -0.6 to $11.3‰$ (one outlier value $= 22.8‰$) for pyrite and from -2.9 to $11.4‰$ for chalcopyrite [*Garuti et al*., 2009].

Schwarzenbach et al. [2012], who performed bulk rock analyses of serpentinites and ophicalcites from the Northern Apennines, found δ^{34}S ranges between -21.7 and $4.3‰$.

Previous bulk mineral studies of sulfides in the HP-serpentinites from the Voltri Massif in Ligurian Alps [*Alt et al*., 2012] and from Monviso in Coattian Alps [*Hattori and Guillot*, 2007] produced δ^{34}S values that can be ascribed to seafloor serpentinization. No evidence of changes in S isotopes can be associated with HP recrystallization in these serpentinites.

Evans et al. [2014] performed in situ S isotope investigations and mapped trace elements of disseminated sulfides in basic eclogites from the Zermatt-Saas Zone and in transitional eclogites from New Caledonia. They found that δ^{34}S in pyrite ranges from $-12‰$ to $17‰$ in the studied samples with variations up to $15‰$ within a single pyrite crystal and, commonly, polymodal distributions of isotopic ratios. They used a combined textural and geochemical approach to interpret the observed isotopic heterogeneities, which were consistent with limited metamorphic reequilibration of S isotopes in the two studied areas. The authors conclude that many of the sulfides from the two localities preserve hydrothermal features, with localized metamorphic recrystallization and, possibly, addition of slab-derived S during the retrogression.

3. Geological Settings

3.1. Beth-Ghinivert

The Beth-Ghinivert deposit lies in the Chisone Valley (Western Alps, Italy; Figure 2) and belongs to the *Schistes Lustrés* Unit of the Piedmont Zone. The *Schistes Lustrés* Unit crops out between the neighboring metasedimentary Brianconnais Unit (to the west) and the underlying Dora-Maira Unit to the east. The *Schistes Lustrés* is a main metasedimentary unit and consists of poly-deformed calcschists (calcareous shales and pelites) that were deposited from late Jurassic onward on the Piedmont Ocean floor [e.g., *Dal Piaz et al*., 1972; *Lemoine et al*., 1986; *Lemoine and Tricart*, 1986]. Meter to kilometer-sized blocks of mafic and/or ultramafic rocks of ophiolitic affinity are scattered within these pelagic sediments, which are part of the internal Penninic Domain [*Dal Piaz et al*., 1972; *Lemoine et al*., 1986; *Lemoine and Tricart*, 1986]. According to several

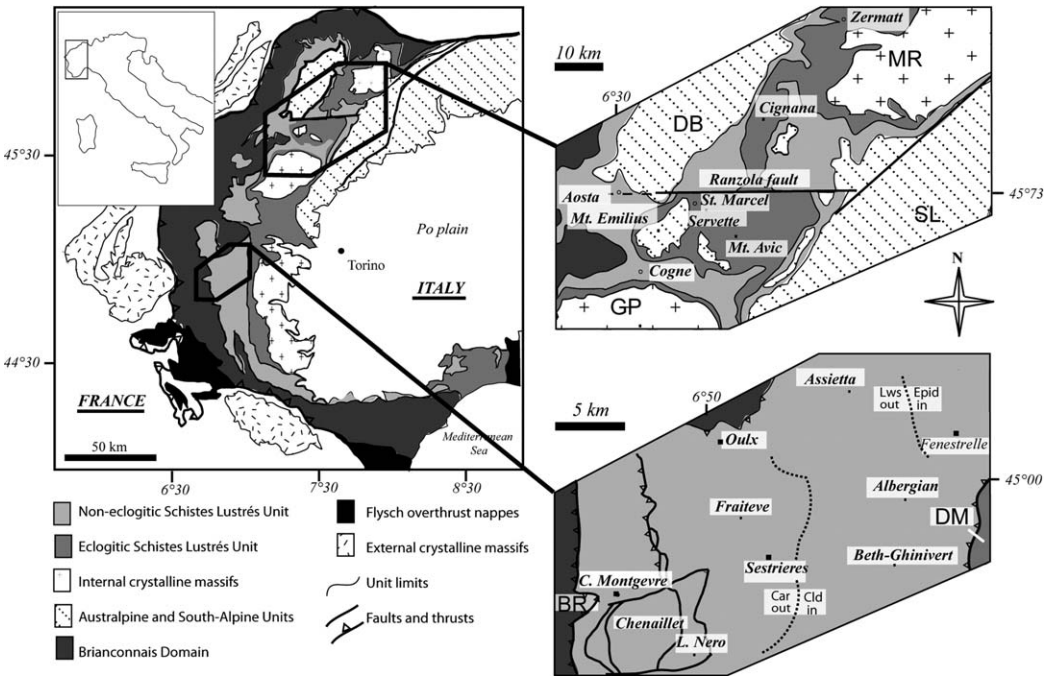

Figure 2. Simplified geological sketch of (left) Western Alps and the detail of the studied zones. (top right) Map of the Servette zone [after *Martin et al*., 2008]. DB = Dent Blanche Unit; GP = Gran Paradiso nappe; MR = Monte Rosa nappe; SL = Sesia-Lanzo zone. (bottom right) Map of the Beth-Ghinivert zone [after *Agard et al*., 2001]. BR= Brianconnais Domain; DM = Dora Maira Massif; car = carpholite; cld = chloritoid; Epid = epidote; Law = lawsonite.

authors [e.g., *Agard et al*., 2001, and references therein], the units belonging to the Penninic Domain underwent subduction during the closure of the Piedmont Ocean [e.g., *Pognante*, 1991; *Agard et al*., 2001; *Tricart and Schwartz*, 2006]. *Agard et al*. [2001] performed a petrologic study of pelitic samples collected between Sestriere and Fenestrelle and suggested that maximum P-T conditions increase significantly from west to east and range from 1.2–1.3 GPa and 300–350°C in the west up to 2.0–2.1 GPa and 450–530°C in the east.

At Beth-Ghinivert, meter to decameter-sized blocks of metabasite occur as scattered irregular bodies within the calcschists and record a polymetamorphic evolution at epidote-blueschist and greenschist-facies conditions. *Giacometti and Rebay* [2013] proposed a metamorphic peak at 1 GPa and 492 ± 35°C followed by reequilibration at 0.82 ± 0.12 GPa and 457 ± 30°C. Relicts of the HP parageneses (blue amphibole, white mica, chlorite, epidote, albite, quartz, minor titanite and, locally, sulfides) survived the retrogression, which occurred at 0.5 ± 0.1 GPa and temperatures below 450°C [e.g., *Agard et al*., 2001].

A 0.25–2.5 m thick zone of pyrite-rich stratiform mineralization is associated with the metabasites (metagabbros, glaucophanites, and greenschist-facies metabasites) and the calcschists [*Novarese*, 1900; *Bouquet and Forette*, 1973; *Giacometti and Rebay*, 2013]. The deposit was exploited during the nineteenth century for copper. *Novarese* [1900] asserted that the mineralized horizon has a lateral extension of at least 400 m (parallel to dip), a mean thickness of 0.5 m, and is continuous, parallel to the direction of strata, to a depth of at least 80 m. Disseminated sulfides occur in the metabasites at the contact with the stratiform mineralization.

According to *Novarese* [1900], the metabasite is locally impregnated by sulfides. At least two different generations of pyrite have been recorded at Beth; common relicts preserving colloidal textures, which are typical low-temperature hydrothermal features, are overgrown by cubic metamorphic pyrite [*Natale*, 1966, 1969; *Natale and Visetti*, 1980]. These features are revealed by chemical etching. A sedimentary-exhalative origin on the Piedmont Ocean floor is proposed for the Beth-Ghinivert deposit [e.g., *Natale and Visetti*, 1980].

3.2. Servette

The Servette deposit lies in the St. Marcel valley (Western Alps, Italy; Figure 2) in the Zermatt Saas Zone of the Penninic Domain. The ophiolites of the Zermatt Saas Zone have been interpreted as oceanic lithosphere

belonging to the Piedmont Ocean, which was subducted below the Apulian margin between ~50 and 40 Ma [e.g., *Lemoine et al*., 1986; *Polino et al*., 1990; *Rubatto et al*., 1998; *Dal Piaz et al*., 2003].

The Zermatt Saas Zone is considered to be composed of ophiolitic slices that recorded different P-T paths during the Alpine orogeny [e.g., *Martin et al*., 2008; *Rebay and Powell*, 2012]. This interpretation is controversial; *Angiboust et al*. [2009] proposed that the Zermatt Saas Zone is a continuous slice of oceanic lithosphere that records relatively homogeneous pressure and temperatures. Exhumation to below 350°C occurred around 44 Ma [*Hunziker*, 1974; *Barnicoat and Cartwright*, 1995].

Servette is the site of an economically exploited Fe-Cu sulfide deposit that has been interpreted as the product of extensive hydrothermal alteration of the seafloor. The rocks underwent eclogite-facies metamorphism, but eclogites sensu stricto (omphacite + garnet rocks) are rare at Servette. Interlayered glaucophanites, chlorite schists, and talc schists are the dominant lithologies [*Castello*, 1981; *Cartwright and Barnicoat*, 1999; *Martin et al*., 2008; *Rebay and Powell*, 2012]. These different rock types have been attributed to different styles of hydrothermal alteration. The talc schists were considered as evidence of up-flow zones in black smoker-type environments, whereas the glaucophanites and chlorite schists formed in zones of downward, up-temperature, pervasive, fluid flow [*Cartwright and Barnicoat*, 1999; *Martin et al*., 2008]. Sulfides at Servette include pyrite, chalcopyrite with accessory sphalerite, bornite, pyrrhotite, neodigenite, marcasite, mackinawite, and rare native copper [e.g., *Tartarotti et al*., 1986; *Krutow-Mozgawa*, 1988; *Martin et al*., 2008].

The sulfide mineralization is concentrated in two major 3–4 m thick layers, and some minor layers (less than 1 m) intercalated between chlorite schists and glaucophanite. Sulfides are also disseminated in the host rocks [*Martin et al*., 2004]. This deposit was exploited from the Middle Ages (or probably Roman times) up to the 1950s with several interruptions of activity [*Martin et al*., 2004].

Martin et al. [2008] proposed a polymetamorphic evolution for Servette, starting with ocean-floor metamorphism followed by Alpine prograde blueschist facies toward peak eclogite-facies metamorphism at 550 ± 60°C and 2.1 ± 0.3 GPa. P-T-peak conditions of 2.3 GPa and 530°C were proposed by *Angiboust et al*. [2009]. The extent of greenschist-facies retrogression is variable at Servette [*Martin et al*., 2008].

4. Methods

4.1. In Situ S Isotope Analyses

Eight samples of massive and disseminated mineralization (six from Servette and two from Beth-Ghinivert) were selected after a detailed petrographic study was performed using transmitted and reflected light microscopy on thin sections and reflected light microscopy on corresponding rock billets. The chosen samples were cut and mounted in EPOFIX epoxy with the in-house pyrite standard Sonora 3.

The mounts were polished with diamond paste down to 0.25 μm, cleaned, and a 30 nm gold coating was applied on the mount surface. In situ analyses (a total of 491 on unknowns and 188 on standards) were performed at the Centre for Microscopy, Characterization and Analysis (CMCA) at The University of Western Australia in Perth (WA) using a CAMECA IMS 1280 ion probe.

Development of the in-house pyrite standard (Sonora 3) is described by *Evans et al*. [2014]. Briefly, Sonora 3 standard is subsamples taken from a 1 cm^3 subsample of pyrite from a large 9 kg cube. The IMS-1280 was used to test the isotopic heterogeneity of the Sonora 3 material, and the absolute $\delta^{34}S$ value obtained by laser fluorination at McGill University is 1.61 ± 0.08‰ relative to VCDT (Vienna Canyon Diablo Troilite).

A 10 keV, 1 nA focused Cs^+ ion beam was used to presputter the analysis area for 10 s before automatic secondary centering and 10 × 4 s analysis cycles were acquired. $^{32}S^-$, $^{33}S^-$, and $^{34}S^-$ secondary ions were collected using Faraday cup detectors and NMR regulation was used for all analyses. An electron gun was used for charge compensation. Other conditions include: 133X magnification between the sample stage and field aperture (FA), 4000 μm FA, 40 eV energy window with a 5 eV offset to the high-energy side, 70 μm entrance slit, and 500 μm exit slits.

All the $\delta^{34}S$ values reported in this paper are referenced to VCDT (Vienna Canyon Diablo Troilite). Matrix corrections for pyrite were made using the laser fluorination $\delta^{34}S$ for the Sonora 3 standard to calculate the IMF on a daily basis. Matrix corrections for chalcopyrite were made using a matrix correction factor for chalcopyrite relative to pyrite obtained from multiple analyses of chalcopyrite on the SIMS IMS 1280 at the

CMCA and laser fluorination measurements of chalcopyrite (n = 5) standard subsamples at McGill University. Further details of the matrix correction procedure are provided by *Evans et al*. [2014].

This in situ microanalytical approach allows evaluation of microscale spatial variation of S isotope values and reveals heterogeneities and/or chemical zoning that record fluid infiltration. S isotopes ratios are reported as δ^{34}S, defined by:

$$\delta^{34}\mathrm{S}\ (‰) = \left\{ \left[\left({}^{34}\mathrm{S}/{}^{32}\mathrm{S}\right)_{\mathrm{sample}} - \left({}^{34}\mathrm{S}/{}^{32}\mathrm{S}\right)_{\mathrm{VCDT}} \right] * \left[\left({}^{34}\mathrm{S}/{}^{32}\mathrm{S}\right)_{\mathrm{VCDT}} \right]^{-1} \right\} * 1000.$$

Average external precision (1 SD) for δ^{34}S analyses of the standards was calculated (for each session day) from the standard deviation of the drift-corrected δ^{34}S values measured in Sonora 3 and range between 0.19 and 0.32‰. Overall, the 188 replicates on the Sonora 3 standard performed as part of this work return a δ^{34}S value of 1.61 ± 0.26‰. Internal precision ranged from 0.14 to 0.30‰ (2σ = 0.28–0.60‰), which is close to the external precision calculated for the Sonora 3 standard.

4.2. EPMA Analyses

Trace element maps for As, Ni, Co, Mn, and Cu for three selected pyrite grains were made to investigate compositional zoning. The maps were obtained using the JEOL 8530F Hyperprobe at the CMCA. Operating conditions were 20 kV accelerating voltage, 100 nA beam current, 50 ms dwell time, and the pixel sizes of 1–2 μm depending on the size and scale of chemical heterogeneity in the area mapped.

4.3. Chemical Etching

After SIMS and EPMA analyses, chemical etching was performed using a 6*M* HNO_3 solution to reveal textural features. The solution was dropped on the mounts and left for 20 min and the mounts were then inspected. This process was repeated until textures were revealed. Observed features were correlated with those detected by in situ S analysis.

5. Petrographic Description

5.1. Samples From Beth-Ghinivert

The two samples from Beth-Ghinivert were collected from an outcrop at one of the mine entrances (44°57′20.87″N 6°59′42.44″E). Sample BE51 comes from a stratiform 30 cm thick massive mineralization at the base of a hectometer-sized metabasite block, which lies within the calcschist sequence. The sample consists of pyrite (∼60 vol %), with tiny sphalerite and rare bornite inclusions, and quartz (∼40 vol %). Chemical etching with 6 mol/L HNO_3 allowed recognition of complex textures related to several growth stages and the local occurrence of metamorphic recrystallization of irregular to polygonal aggregates (Figure 3a).

Sample BE66 was collected at the top of the stratiform 30 cm thick massive mineralization (where BE51 comes from), at the contact with the metabasite. This sample consists of two regions with different modal composition and textural features. The first region consists of mostly euhedral to rounded pyrite (∼59 vol %) that contains frequent bornite, chalcopyrite, sphalerite, and a few pyrrhotite inclusions, generally anhedral chalcopyrite (∼40 vol %), minor quartz (∼1 vol %), and accessory magnetite (Figure 3b). The second region is composed of chlorite (∼40 vol %), quartz (∼40 vol %), minor fine-grained sulfides (pyrite and chalcopyrite; ∼20 vol %), and accessory white mica (Figure 3c). The mineralization is moderately deformed, but folding and kink-banding occur in the silicate-rich portion at its margins (Figure 3c). We focused our attention on the sulfide-rich portion of the sample, where crystals were large enough to be studied in detail.

5.2. Samples From Servette

Six samples were analyzed from four lithologies (chlorite schist, glaucophanite, talc schist, and massive mineralization). Samples come from the talus located between N45°42.111′, E7°27.327′ (alt. 1820 m) and N45°42.066′, E7°27.280′ (alt. 1792 m) as the mine is no longer accessible.

Samples belonging to the same rock type differ in their mineral modal compositions. Sulfides occur in all the samples investigated in the matrix and as inclusions in garnet porphyroblasts. Both sulfide textural positions are associated with prograde to peak condition parageneses, which are locally overgrown by retrograde assemblages [*Kawakami et al*., 2006; *Martin et al*., 2008].

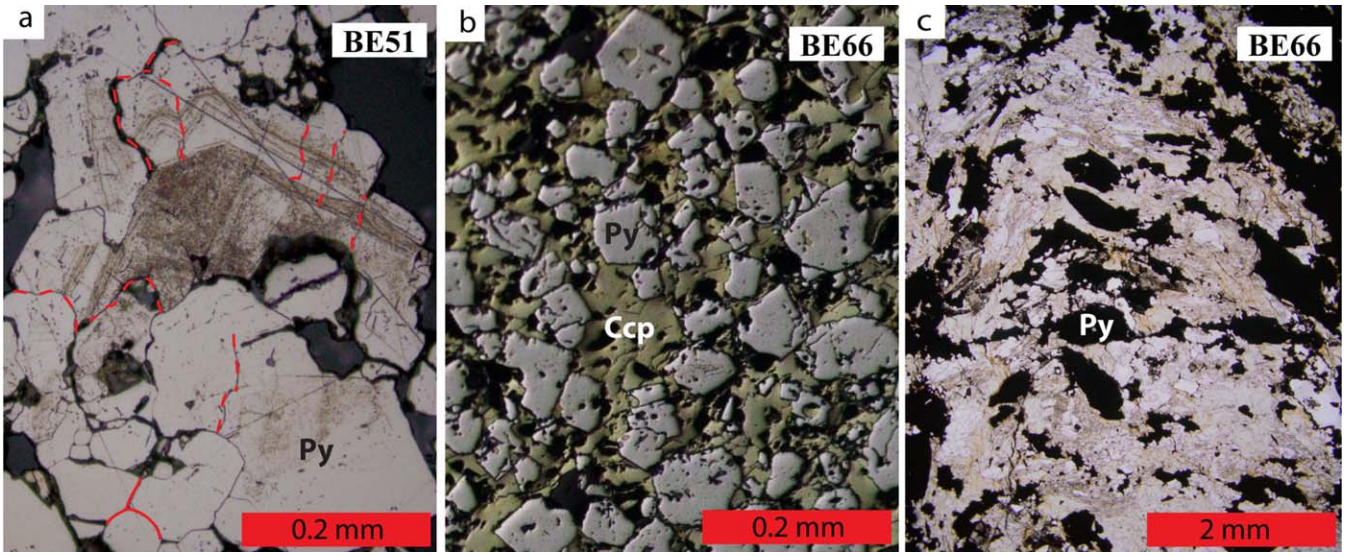

Figure 3. (a and b) Reflected and (c) transmitted plane-polarized light microscope images of the samples from Beth-Ghinivert. (Figure 3a) Sample BE51; pyrite aggregates in a quartz matrix: chemical etching evidences relict growth structures (Figure 3b) in pyrite and local recrystallized irregular (see red dotted lines) to polygonal aggregates (see red solid lines). (b) Sample BE66; cubic pyrite and anhedral chalcopyrite. Absence of polygonal aggregates. (Figure 3c) Sample BE66; chlorite-quartz-pyrite folded layers at the very contact between the massive mineralization and the country metabasite. Pyrite crystals are deformed with locally resorbed margins. Irregular sulfide crystals fill the space among blastic silicates. Ccp = chalcopyrite; Py = pyrite.

Samples SE13 and SE14 are from garnet-bearing chlorite schists. These samples consist mostly of chlorite (up to 60 vol %) with up to centimeter-sized garnets (~23 vol %), sulfides (~10 vol %, pyrite and chalcopyrite with rare tiny sphalerite and galena inclusions), quartz (~5 vol %), chloritoid porphyroblasts (~2 vol %), and accessory talc, albite, rutile (rimmed by ilmenite), blue amphibole (only in SE13), and late magnetite (Figures 4a and 4b). The garnet crystals are zoned with respect to inclusion assemblages. Quartz, titanite, pyrite, and chalcopyrite inclusions are aligned along a relict foliation in the core of garnets. Scattered quartz, pyrite, talc, and rutile (rimmed by ilmenite) inclusions occur at the rim of crystals. Chloritoid and garnet rims are partially replaced by late chlorite, which also occurs with magnetite in fractures within porphyroblasts.

In the matrix, chlorite, quartz, pyrite (which includes rutile), minor chalcopyrite, and rare blue amphibole in SE13 are aligned parallel to the pervasive HP foliation. Quartz, chlorite, and talc (±blue amphibole and albite in SE13) occur in the pressure shadows of garnet and chloritoid porphyroblasts.

Sample SE8 is a garnet-bearing glaucophanite. Garnet (~30 vol %), chloritoid porphyroblasts (~5 vol %), and pseudomorphs after lawsonite porphyroblasts (consisting of epidote, phengite, paragonite, and albite; ~20 vol %) occur within a foliated matrix made of glaucophane (~33 vol %), clinozoisite (~4 vol %), and talc (~5 vol %). Garnet and chloritoid are up to 9 mm in diameter and are partially replaced by late chlorite at crystal rims and along fractures where rare tiny magnetite crystals were found. Garnets include rutile (locally rimmed by ilmenite), quartz, glaucophane, rare talc, and pyrite. These phases locally define a spiral internal foliation that testifies that garnet porphyroblasts grew simultaneously with the development of the external foliation. Rutile in garnet and chloritoid both includes and is included by sulfides. Pyrite (~2 vol %), chalcopyrite (~1 vol %), and rare bornite and sphalerite in the matrix are stable with garnet, glaucophane, chloritoid, rutile, and clinozoisite (Figure 4c).

ATSV-001 is a garnet-sulfide-rich talc schist (Figure 4d), with 2–5 mm diameter garnet (~40 vol %), pyrite (~25 vol %), chalcopyrite (~5 vol %), felty-looking talc (~20 vol %), and chlorite (~10 vol %) and accessory quartz. The garnet forms a framework of subequant grains. Pyrite occurs as submillimeter inclusions in garnet and with chlorite found in cracks in garnet. Polygranular patches of pyrite up to a few mm across occur in the matrix. Chalcopyrite typically surrounds matrix pyrite (Figure 4d) and is occasionally intergrown with silicates without pyrite. Talc, which is often iron stained, occurs in felty, deformed masses between pyrite grains. Chlorite occurs on the rims of garnet, and as laths that crosscut talc. Rutile, rimmed by ilmenite, is included in garnet and contains fine exsolution laminae and blebs of hematite.

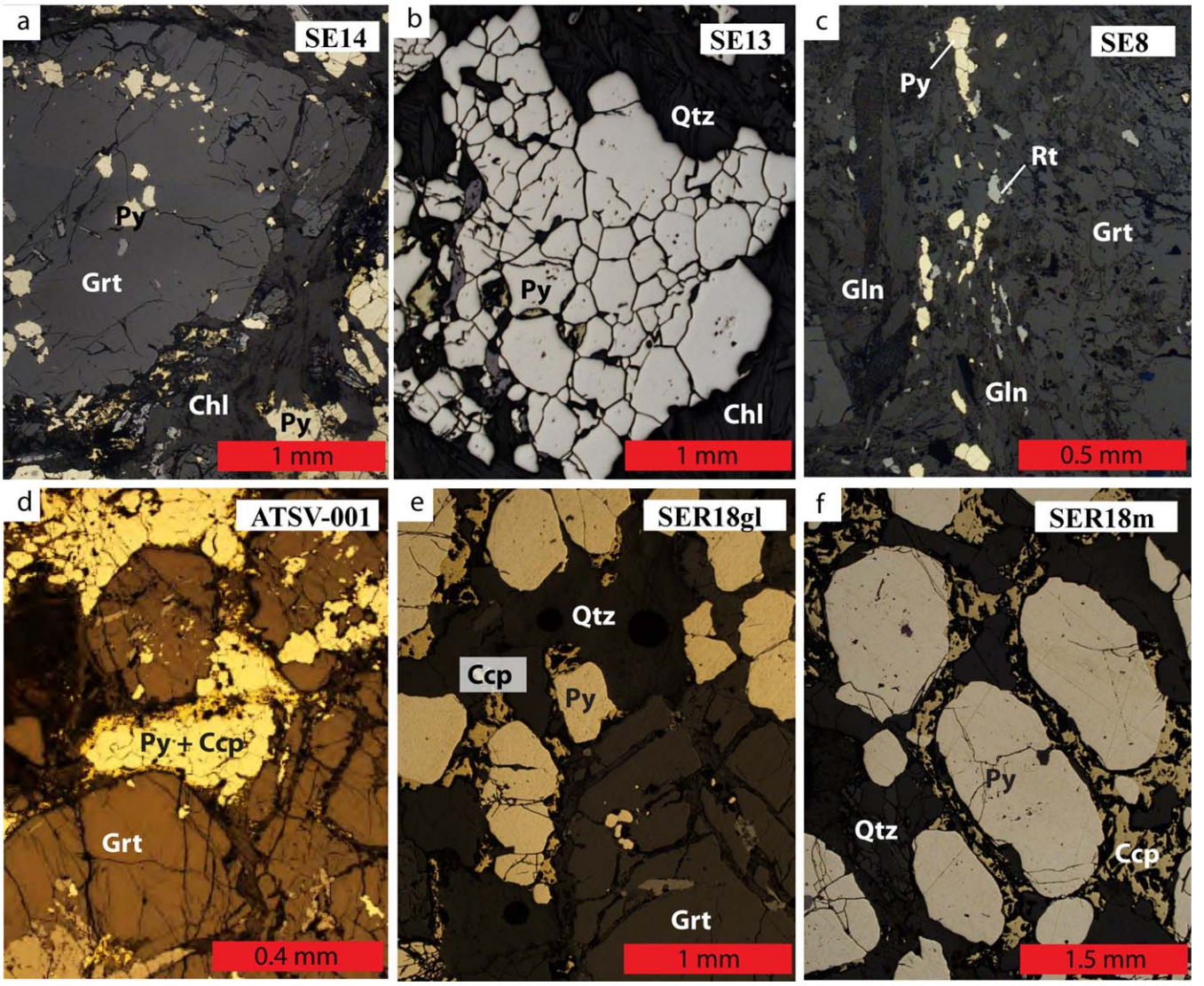

Figure 4. Reflected plane-polarized light microscope images of some of the samples from Servette. (a) Sample SE14; garnet including pyrite, chalcopyrite, and rutile, some of which are far from fractures occurring within the host mineral; pyrite and chalcopyrite also widespread in the chlorite matrix. (b) Sample SE13; polygonal pyrite (and subordinate chalcopyrite and quartz) aggregate in the chlorite matrix. (c) Sample SE8; pyrite and subordinate chalcopyrite in the glaucophane matrix. Garnet porphyroblasts occur in the right side of the picture. (d) Sample ATSV-001; pyrite and chalcopyrite occur both as small inclusions in garnet porphyroblasts and as polygonal aggregates in the matrix. (e) Sample SER18gl; pyrite and chalcopyrite-rich glaucophanite: sulfides occur both included in garnet and in the matrix. (f) Sample SER18m; rounded pyrite crystals surrounded by anhedral chalcopyrite in a quartz matrix. Ccp = chalcopyrite; Chl = chlorite; Gln = glaucophane; Grt = garnet; Py = pyrite; Qtz = quartz; Rt = rutile.

Sample SER18 contains the contact between a massive pyrite-chalcopyrite glaucophanite (SER18gl; Figure 4e) and a garnet and sulfide-bearing mineralization (SER18m; Figure 4f).

The glaucophanite (SER18gl) is mainly made of glaucophane (~35 vol %), garnet (~30 vol %), pseudomorphs after lawsonite (consisting of epidote, phengite, paragonite, and albite ~17 vol %), sulfides (pyrite with subordinate chalcopyrite and rare bornite; ~16 vol %), minor quartz, and chlorite and accessory talc. Chalcopyrite is present both in the matrix and as inclusions in garnets whereas pyrite is common in the matrix, but only a few micrometer-sized inclusions occur in garnet (Figure 4e).

The massive mineralization (SER18m) is mainly made up of pyrite (~45 vol %), garnet (~25 vol %), chalcopyrite (~15 vol %), and quartz (~15 vol %). Rutile rimmed by ilmenite occurs as an inclusion in garnet in both SER18gl and SER18m. The modal abundance of garnet increases toward the contact with the metabasite. Pyrite is present both in the matrix and as inclusions in garnet whereas only interstitial chalcopyrite is

Table 1. Lowest, Highest, and Average $\delta^{34}S$ Values (‰), Standard Deviations (‰), and Number of Analyses for Pyrite (Py) and Chalcopyrite (Ccp) From the Eight Studied Samples[a]

		Lowest $\delta^{34}S$ (‰)	Highest $\delta^{34}S$ (‰)	Average $\delta^{34}S$ (‰)	σ (‰)	Number of Analyses
SE 14	py in garnet	0.6	8.1	6.2	1.3	35
	py matrix	−2.0	7.6	5.1	1.9	28
	ccp matrix	−1.6	1.3	−0.7	0.8	10
SE 13	py in garnet	3.3	8.4	5.2	1.5	35
	py matrix	2.4	6.3	4.1	0.7	57
	ccy in garnet	−0.9	2.1	−0.2	0.7	12
	ccy matrix	−0.7	−0.3	−0.5	0.2	4
	ccy vein	−2.1	−0.6	−1.4	0.6	4
SE 8	py in garnet	−0.9	2.4	0.8	1.6	2
	py matrix	8.1	13.9	9.5	1.5	39
	ccp matrix	0.9	0.9			1
ATSV-001	py in garnet	7.2	9.6	8.7	0.8	7
	py matrix	6.8	12.6	8.1	1.3	28
	ccp matrix	1.6	2.7	2.2	0.4	6
	ccp vein	2.2	3.0	2.5	0.2	12
SER18 gl	py matrix	−2.3	7.1	2.9	2.9	21
	ccp in garnet	−4.0	−3.6	−3.8	0.2	8
	ccp matrix	−3.8	−3.0	−3.3	0.3	7
SER18 min	py in garnet	−0.8	−0.1	−0.5	0.2	8
	py matrix	0.1	1.2	0.8	0.2	27
	ccp matrix	−3.4	−1.2	−1.9	0.6	9
BE51	py	−1.4	6.4	3.6	1.6	56
BE66	py	−0.7	3.8	1.7	0.9	61
	ccp	−6.7	−4.6	−5.2	0.6	14

[a]Data are reported for pyrite (py) and chalcopyrite (ccp) in each different microstructural domain (i.e., sulfide in the matrix or included in garnet).

present in the matrix. The pyrite crystals (up to 2 mm) in the matrix have rounded margins suggesting resorption (Figure 4f).

6. Isotope Characterization

Minimum, maximum, and average $\delta^{34}S$ values, standard deviations, and the number of analyses are summarized in Table 1.

6.1. Samples From Beth-Ghinivert

6.1.1. BE51 (Massive Mineralization)

The $\delta^{34}S$ of pyrite ranges from −1.4 to 6.4‰ within a distance of 1 mm (Figures 5a, 5b, and 6a and Table 1). There is no obvious correlation between isotopic variations and growth textures or with textures related to metamorphic recrystallization (Figures 5a–5c).

Qualitative element mapping shows that the concentration of Mn shows a pattern consistent with growth zoning (Figure 5d). However, $\delta^{34}S$ values in the same aggregate of pyrite crystals are scattered and do not correlate with Mn distribution (Figure 5d). Metamorphic recrystallization textures are not related to Mn zoning and growth textures or to sulfur isotopes variations.

6.1.2. BE66 (Mineralization Close to the Country Rock)

The $\delta^{34}S$ value ranges from −0.7 to 3.8‰ in pyrite (average value = 1.7‰ ± 0.9‰, n = 61) and from −6.7 to −4.6‰ (average value = −5.2 ± 0.6‰, n = 14) in chalcopyrite (Figure 6b and Table 1). $\delta^{34}S$ values vary by up to 3.4‰ within a single pyrite crystal. In one pyrite crystal (Figure 5e), isotopic zoning occurs, with lower $\delta^{34}S$ values at the crystal core. In this sample, chalcopyrite inclusions in pyrite and chalcopyrite in the matrix record statistically undistinguishable $\delta^{34}S$ values. $\Delta_{av.py\text{-}ccp}$ is 6.9 ± 1.4‰.

Qualitative trace element mapping of the pyrite shows that only Co varies to a detectable degree within the crystal. The lowest $\delta^{34}S$ values observed in pyrite (−0.7 ± 0.4‰ to 0.8 ± 0.2‰) correspond to the Co-rich core of a 2 mm sized crystal. This low-$\delta^{34}S$ and Co-rich core is overgrown by a high-$\delta^{34}S$ zone that is characterized by cyclical variations of Co content (Figure 5f).

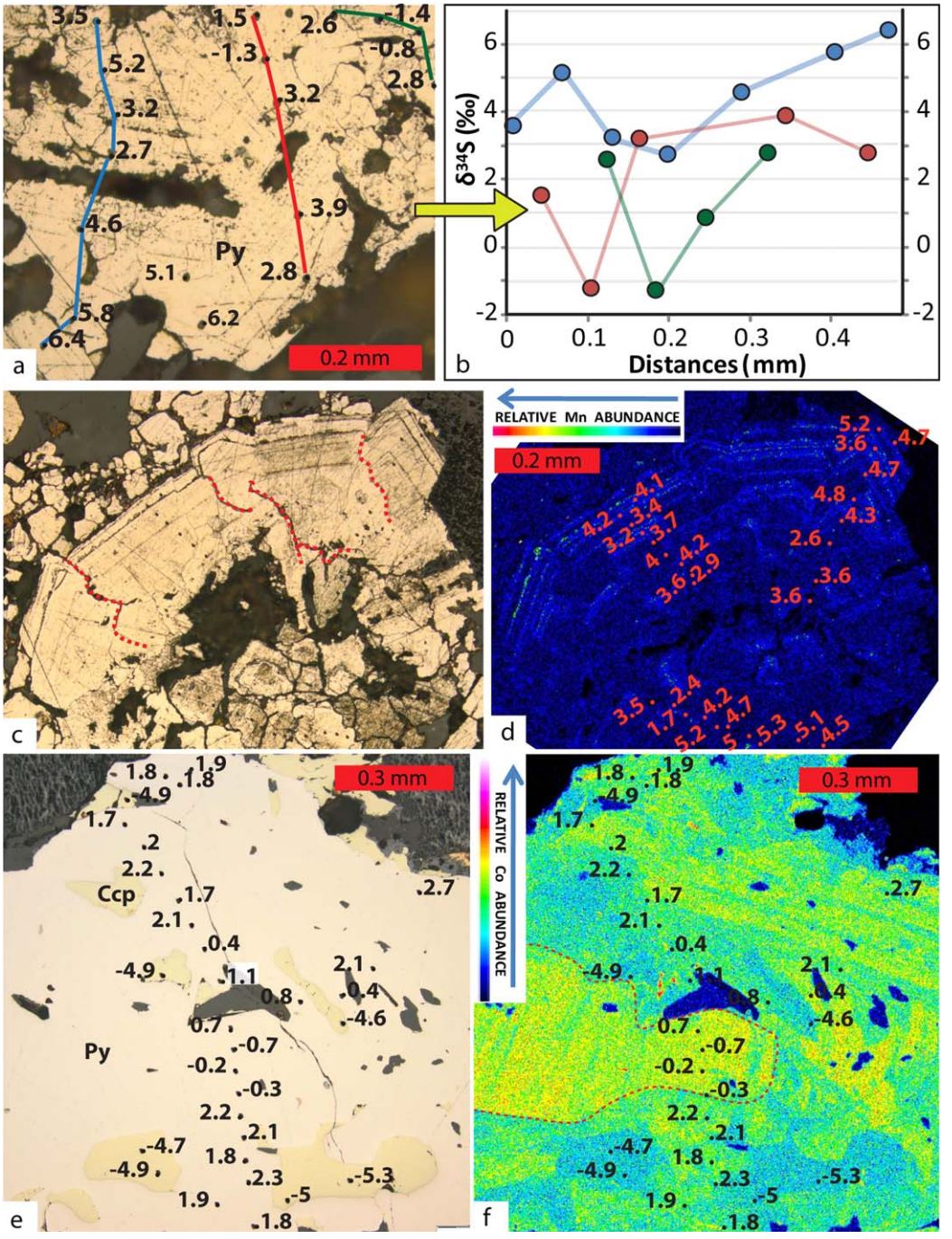

Figure 5. Textures and geochemical features in samples from Beth-Ghinivert. Numbers indicate the measured δ^{34}S values. (a) Sample BE51; pyrite aggregate preserving growth textures. (b) The diagram shows the variation of δ^{34}S along three transects highlighting the isotopic heterogeneity of pyrite within a few tens of microns. (c) Sample BE51; well-preserved growth textures correspond to a zoned distribution of Mn (shown in Figure 5d). Recrystallization is localized (see red dotted lines indicating boundaries). (d) Sample BE51; relative distribution of Mn in pyrite, mimicking growth textures and evidencing lack of metamorphic rehomogenization of trace elements. (e) Sample BE66; low δ^{34}S values occur at the core of this pyrite crystal, whereas higher δ^{34}S values occur at the rim. (f) Sample BE66; the distribution of Co evidences relict growth textures. Dotted red lines evidence Co-rich cores (warm colors), which record low δ^{34}S values. Oscillation of Co relative concentration is seen at crystal rims where higher δ^{34}S values occur.

6.2. Samples From Servette

6.2.1. SE13 and SE14 (Chlorite Schists)

δ^{34}S values were measured in pyrite and chalcopyrite from both samples (Figures 7a–7c and 8a–8e and Table 1). δ^{34}S values for pyrite inclusions in garnet (Figures 8a and 8d) and pyrite in the matrix (Figures 8b

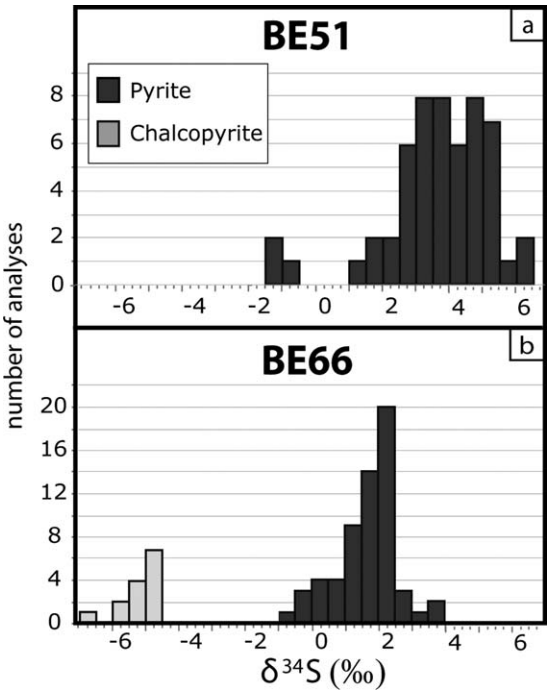

Figure 6. Histograms showing the distribution of δ^{34}S values observed in the samples from Beth-Ghinivert. (a) Sample BE51; wide range of δ^{34}S values for pyrite. (b) Sample BE66; δ^{34}S values for pyrite and chalcopyrite.

and 8e) span the same range of 2–8.5‰ (excluding two outliers in SE13 at −2.0 and 0.6‰). Samples were heterogeneous with respect to sulfur isotopes on the micron scale; δ^{34}S is homogeneous at the submillimeter scale only within totally recrystallized pyrite aggregates in the matrix.

The δ^{34}S values of the two different textural positions in the two samples are statistically indistinguishable. However, pyrite included in garnet records slightly heavier average isotopic compositions than pyrite in the matrix. Average δ^{34}S values in SE13 are 5.2 ± 1.5‰ (n = 35) and 4.1 ± 0.7‰ (n = 57), respectively, for pyrite inclusions in garnet and pyrite in the matrix. In sample SE14, average δ^{34}S are 6.2 ± 1.3‰ (n = 35) and 5.1‰ ± 1.9‰ (n = 28), respectively, for pyrite inclusions in garnet and pyrite in the matrix (Figures 8a–8e and Table 1). δ^{34}S is homogeneous at the submillimeter scale only within totally recrystallized pyrite aggregates in the matrix.

δ^{34}S in chalcopyrite is more homogeneous than in pyrite (Figure 8) and, as for pyrite, the average values are statistically indistinguishable. In sample SE13, the average δ^{34}S for chalcopyrite in garnet is −0.2 ± 0.7‰ (n = 12); δ^{34}S for chalcopyrite in the matrix is −0.5 ± 0.2‰ (n = 4), and the average δ^{34}S for chalcopyrite in a vein crosscutting a garnet porphyroblast is −1.4 ± 0.6‰ (n = 4; Figures 8a–8c). In sample SE14, chalcopyrite inclusions were smaller than the ion probe beam and were not analyzed. Average δ^{34}S for chalcopyrite from the matrix in SE14 is −0.7 ± 0.8‰ (n = 10; Figure 8e). The $\Delta_{av.py\text{-}ccp}$ (=average $\delta^{34}S_{pyrite}$ – average $\delta^{34}S_{chalcopyrite}$) value in garnet inclusions is 5.4 ± 1.7‰ in sample SE13; the $\Delta_{av.py\text{-}ccp}$ values in the matrix are 4.6 ± 0.9‰ and 5.8 ± 2.7‰ in SE13 and SE14, respectively.

Nonquantitative minor element maps of pyrite aggregates in the matrix of SE14 reveal that only Co, and to some extent As, show heterogeneous distributions (Figure 7c). The lowest δ^{34}S values correspond to the

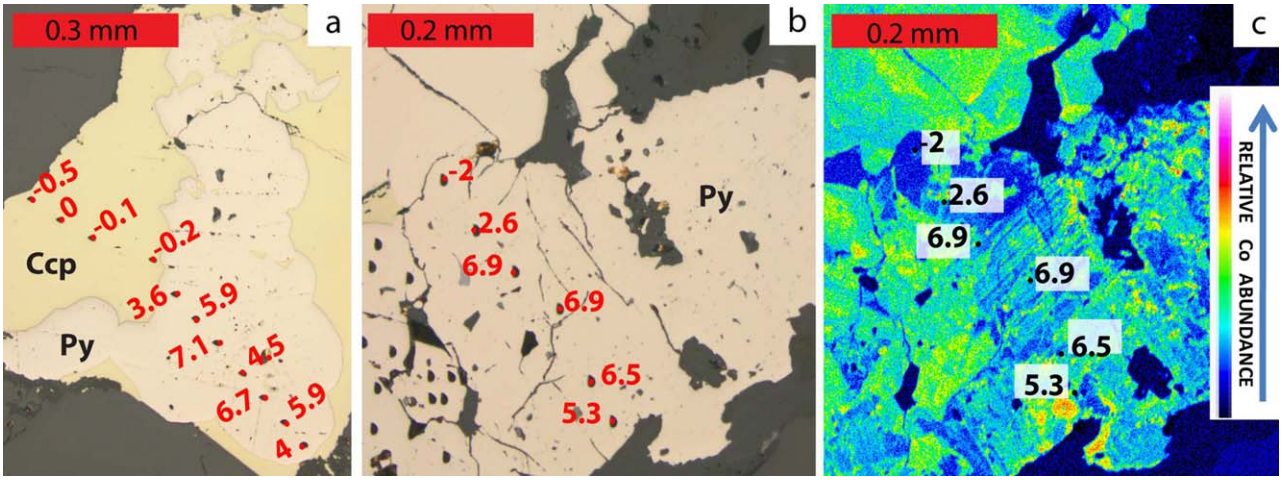

Figure 7. δ^{34}S values (‰) in some of the studied microsites in chlorite schists for pyrite (py) and chalcopyrite (ccp). (a) Sample SE13; pyrite and chalcopyrite included in garnet. Heterogeneous δ^{34}S values occur in pyrite, in contrast to the relative homogeneity in chalcopyrite. (b) Sample SE14; pyrite aggregate in the matrix with wide δ^{34}S range. (c) Qualitative Co distribution in the aggregate of Figure 3b. Later pyrite is Co poor (cool colors) in comparison to pyrite deposited earlier (warm colors). Ccp = chalcopyrite; Py = pyrite.

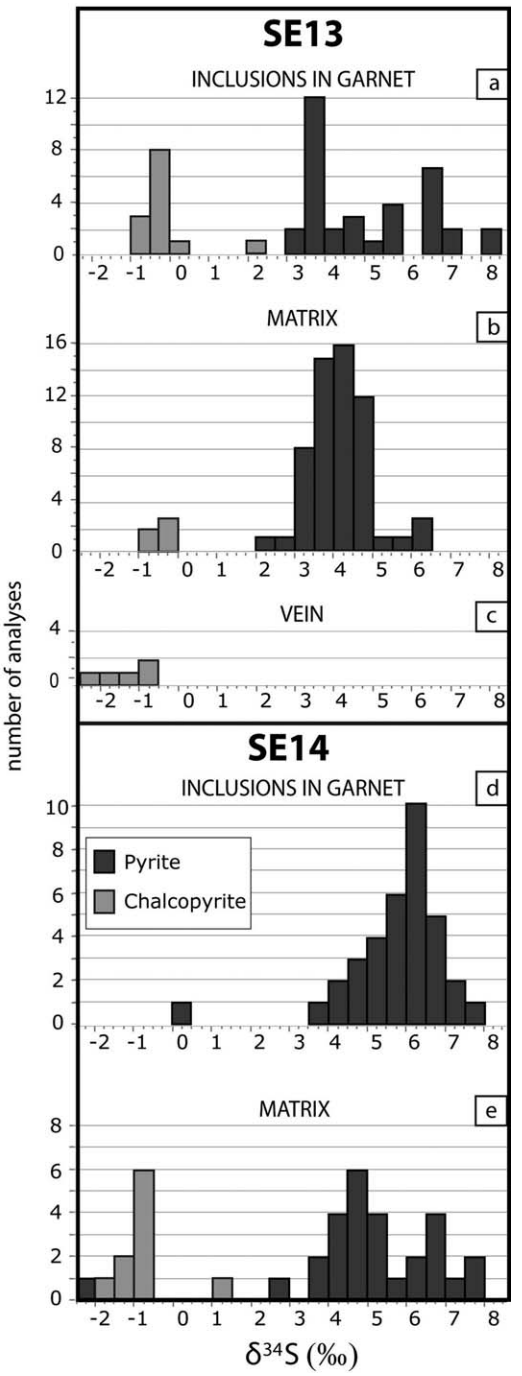

Figure 8. Histograms showing the distribution of $\delta^{34}S$ values observed in chlorite schists. Note the different scales of the histograms for appropriate comparison. Light gray is chalcopyrite (ccp) and dark gray is pyrite (py). Pyrite is isotopically heterogeneous compared to chalcopyrite at the sample scale. (a) Sample SE13; sulfide inclusions in garnet. (b) Sample SE13; matrix sulfides. (c) Sample SE13; chalcopyrite in a vein crosscutting a garnet blast. (d) Sample SE14; pyrite inclusions in garnet. (e) Sample SE14; matrix sulfides.

lowest Co-As abundance, and texturally late Co-rich pyrite is partially replaced by Co-poor pyrite, but there is no consistent correlation between the Co-As distribution and $\delta^{34}S$.

6.2.2. SE8 (Glaucophanite)

$\delta^{34}S$ measured in pyrite from the matrix (average $9.5 \pm 1.5‰$, n = 39; Figure 9a and Table 1) is significantly heavier than $\delta^{34}S$ observed in the few tiny pyrite inclusions in garnet (-0.8 and $2.4‰$; Figure 10a and Table 1). Values measured in the matrix are mostly in the 8–10‰ range with four analyses around 13–14‰, and variations up to 5.8‰ within a 60 μm crystal (Figures 9a and 10d).

Only one chalcopyrite crystal in the matrix was large enough to be analyzed. Its $\delta^{34}S$ is 0.9‰, which gives a $\Delta_{py\text{-}ccp}$ of $8.6 \pm 1.5‰$ if this value is compared with the average $\delta^{34}S$ of pyrite from the matrix.

6.2.3. ATSV-001 (Talc Schist)

Pyrite $\delta^{34}S$ is relatively spatially homogeneous. Most values that lie between 6.5 and 8.5‰, with the exception of two outliers from two analyses within a few 10 s of microns of each other which display heavier $\delta^{34}S$ values of around 12‰ (Figures 9b, 9c, and 10c–10e and Table 1). The average $\delta^{34}S$ for pyrite in garnet and in the matrix (including the outliers) are, respectively, $8.7 \pm 0.8‰$ (n = 7) and $8.1 \pm 1.3‰$ (n = 28; Figures 10c and 10d and Table 1). Chalcopyrite, as in other samples, is more homogeneous than pyrite (Figures 9b and 10d–10e). The average $\delta^{34}S$ is $2.2 \pm 0.4‰$ (n = 6) in the matrix and $2.5 \pm 0.2‰$ (n = 12) in a later vein (Figures 10d–10e). The $\Delta_{av.py\text{-}ccp}$ value in the matrix is $5.9 \pm 1.7‰$.

There is no evidence of a systematic relationship between pyrite $\delta^{34}S$ values and location within the grain or with proximity to chalcopyrite (Figure 9b). Apart from two high $\delta^{34}S$ values recorded in the matrix, which were rechecked and found to be robust, the isotopic composition in garnet inclusions and in the matrix are statistically undistinguishable (see Table 1).

6.2.4. SER18gl (Glaucophanite)

Pyrite is widespread in the matrix (Figure 11a), but only a few very small inclusions occur in garnet and these were too small (<10 μm) to be analyzed. $\delta^{34}S$ in pyrite is partially heterogeneous; values range from -2.3 to $+7.1‰$ within a single matrix pyrite crystal: the average $\delta^{34}S$ value is $2.9 \pm 2.9‰$ (n = 21; Figure 11a).

Matrix pyrite exhibits three modes of $\delta^{34}S$ values (Figures 11a and 12b). The first is represented by negative $\delta^{34}S$ values and is only found in the core of crystals in the matrix. The other two groups, with values of

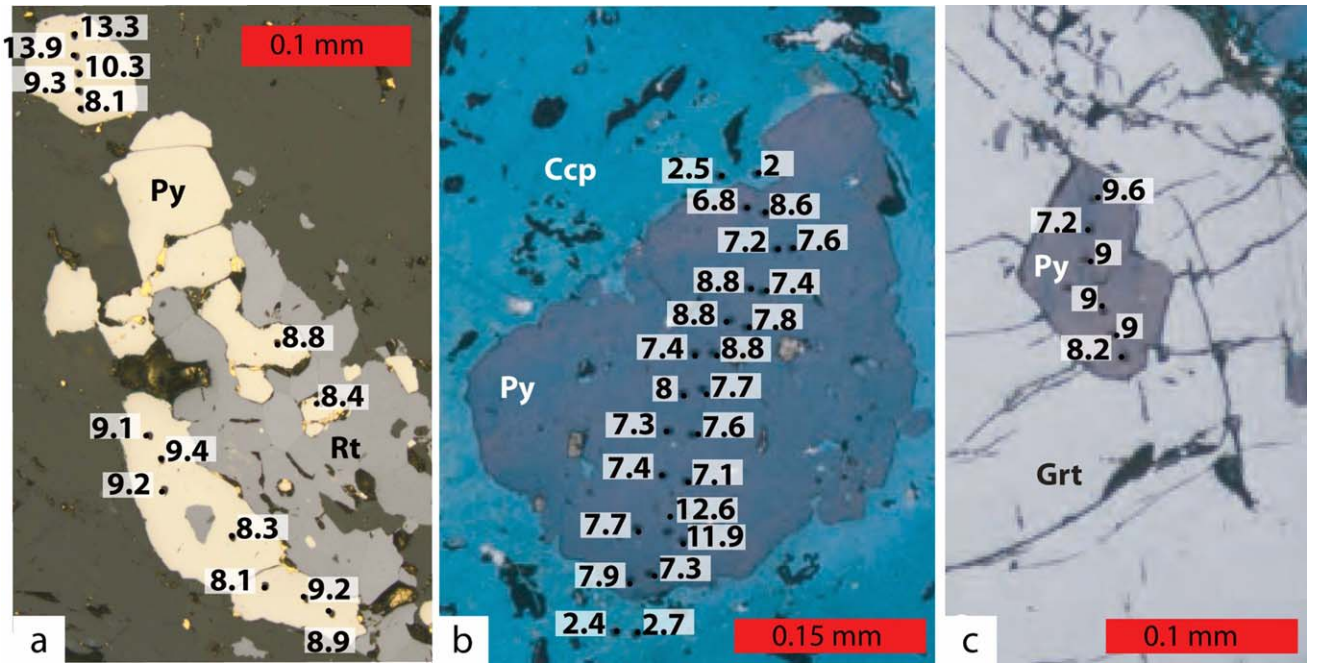

Figure 9. $\delta^{34}S$ values (‰) in some of the studied samples. (a) Sample SE8 (glaucophanite); pyrite intergrown with rutile in the metamorphic peak foliation. (b) Sample ATSV-001 (talc schist); pyrite rimmed by chalcopyrite in the matrix. $\delta^{34}S$ values of the pyrite and chalcopyrite are homogeneous except for two outlying high values in the pyrite. (c) Tiny pyrite inclusions in garnet. ATSV-001. Ccp = chalcopyrite; Py = pyrite; Ru = rutile.

3–4‰ and 5–7.1‰, respectively, occur in the rim of the same pyrite crystal as that in which the lowest values are observed.

In chalcopyrite, $\delta^{34}S$ is relatively spatially homogeneous ranging from −4 to −3.6‰ in garnet inclusions (average $\delta^{34}S = -3.8 \pm 0.2$‰, n = 8; Figure 12a) and from −3.4 to −3‰ in the matrix (average $\delta^{34}S = -3.3 \pm 0.3$‰, n = 7; Figure 12b and Table 1). The $\Delta_{av.py\text{-}ccp}$ value in the matrix is 6.2 ± 3.1‰.

6.2.5. SER18m (Massive Mineralization)

The $\delta^{34}S$ of pyrite included in garnet shows little spatial variability and ranges from −0.8 to −0.1‰ with an average of −0.5 ± 0.2‰ (n = 8; Figure 12c). The $\delta^{34}S$ of pyrite in the matrix ranges from 0.1 to 1.2‰ (n = 27; Figures 11b and 12d): the average is 0.8‰ ± 0.2‰. The $\delta^{34}S$ of chalcopyrite from the matrix ranges from −2 to −1.2‰ with a single low outlier of 3.4‰ and an average of −1.9‰ ± 0.6‰ (n = 9). The $\Delta_{av.py\text{-}ccp}$ value in the matrix is 2.7 ± 0.8‰.

The isotopic compositions of pyrite in garnet, pyrite in the matrix, and chalcopyrite in the matrix are significantly different and rather homogeneous within each category ($1\sigma \leq 0.6$‰; Table 1). This is in contrast with observation from the host rock SER18gl, where pyrite in the matrix is extremely heterogeneous.

7. Discussion

7.1. Length Scales of Sulfur Isotopic Disequilibrium

The combined textural and isotopic investigation shows that isotopic equilibrium at Servette and Beth-Ghinivert occurs on very limited length scales, if at all:

1. In both deposits, the $\delta^{34}S$ composition of pyrite is heterogeneous (with variations up to 9.4‰ at Servette and up to 7.8‰ at Beth-Ghinivert) at the submillimeter scale, indicating limited length scales of equilibrium (Figures 5a, 5b, and 11). Mean $\delta^{34}S$ values in a given sample have 1σ standard deviations up to 2.9‰, which are greater than the internal precision of the analyses (2σ = 0.28–0.62‰; see section 4.1 and Table 1).

2. Sulfur isotope in chalcopyrite may have reequilibrated on longer length scales than in pyrite. Chalcopyrite is relatively homogeneous on the mm scale in any sample with 1σ standard deviations in the 0.2–0.8‰ range (Table 1).

3. Chalcopyrite and pyrite are not in isotopic equilibrium. Even taking into account the propagation of errors in calculating $\Delta_{av.py\text{-}ccp}$ and considering the lowest possible values for each sample, $\Delta_{av.py\text{-}ccp}$ is generally greater

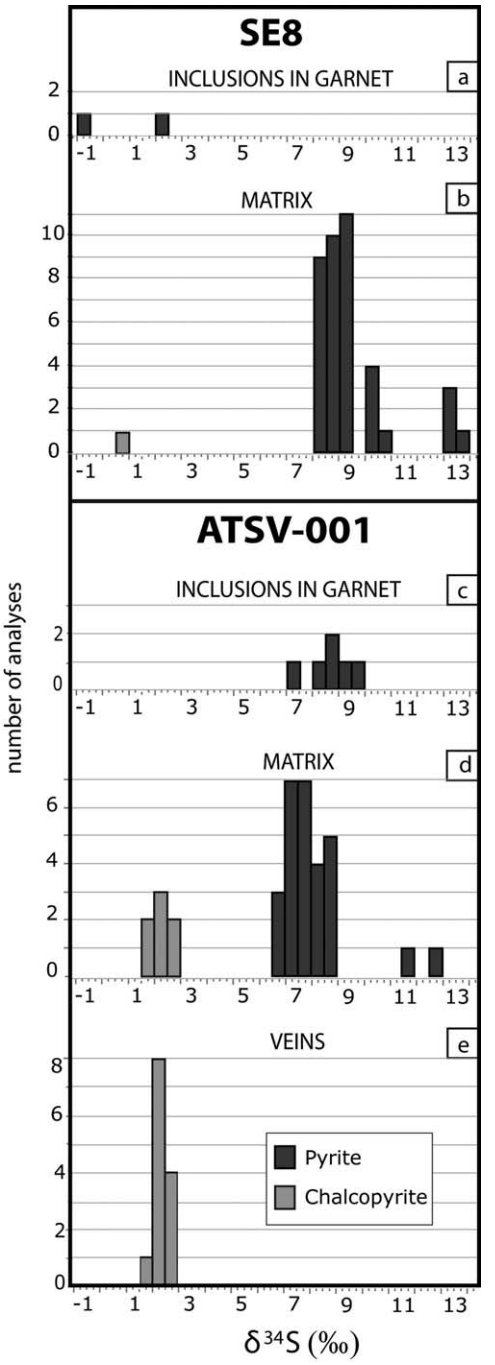

Figure 10. Histograms showing the distribution of δ^{34}S values observed in (a and b) SE8 and (c–e) ATSV-001. Note the different scales of the histograms for appropriate comparison. Light gray is chalcopyrite (ccp) and dark gray is pyrite (py). (Figure 10a) Pyrite inclusions in garnet with low δ^{34}S values. (Figure 10b) Matrix pyrite mainly ranges between 8 and 10‰. (Figure 10c) Pyrite inclusions in garnet and chalcopyrite in a vein (Figure 10e) are isotopically similar to the corresponding minerals in the matrix (Figure 10d).

than 3.1‰ at both deposits, with values up to 10.1‰. These values are higher than those expected at either the peak temperature proposed for Servette (i.e., T = 550 ± 60°C) [*Martin et al.*, 2008] and Beth-Ghinivert (492 ± 35°C) [*Giacometti and Rebay*, 2013] and at greenschist-facies retrogression temperatures around 300°C (Figure 13). At these temperatures, $\Delta_{av.py\text{-}ccp}$ is expected to be 0.8‰, 0.9‰, and 1.4‰, respectively, based on fractionation factors reported by *Seal* [2006] (see references therein for details). $\Delta_{av.py\text{-}ccp} > 6$‰ requires temperatures below 0°C which are not likely, even for processes occurring at the ocean floor.

7.2. Preservation of Protolith Isotopic Composition

The limited length scale of isotopic equilibrium observed at Servette and Beth-Ghinivert may have been inherited from the protolith or have developed during metamorphism. At Beth-Ghinivert, primary pyrite growth textures are widespread and unaffected by the limited metamorphic recrystallization. Analogous textures were described by several authors in sulfides at Beth-Ghinivert [*Natale*, 1966, 1969; *Natale and Zucchetti*, 1966; *Natale and Visetti*, 1980] and were interpreted as ocean-floor relicts.

Metamorphic recrystallization appears not to have caused homogenization of Mn and Co growth zoning so δ^{34}S values are likely to reflect those inherited from the ocean floor (Figure 5). Deformation and metamorphic mobilization of sulfides are extremely localized (millimeter scale) and are always coupled (Figure 3c). Their mutual occurrence supports an important role for deformation in mobilization of S, as has been suggested for other metamorphosed VMS deposits [*Marshall and Gillian*, 1993; *Tomkins*, 2007].

We therefore propose that most textural and isotopic features at Beth-Ghinivert were produced during ocean-floor metasomatism and that the limited extent of deformation-induced sulfur remobilization is responsible for the preservation of these primary features.

7.3. S Isotopes Records of Metamorphic Processes

7.3.1. Heterogeneous Pyrite

At Servette, metamorphic textures are widespread in sulfides (Figure 4b). In samples SE8, SE14, and SER18gl, pyrite in garnets and some matrix pyrite cores record different compositions compared to pyrite rims in the matrix (Figures 7b, 9a, and 11 and Table 1). These texturally distinct δ^{34}S populations in pyrite cannot be explained without metamorphic redistribution of δ^{34}S.

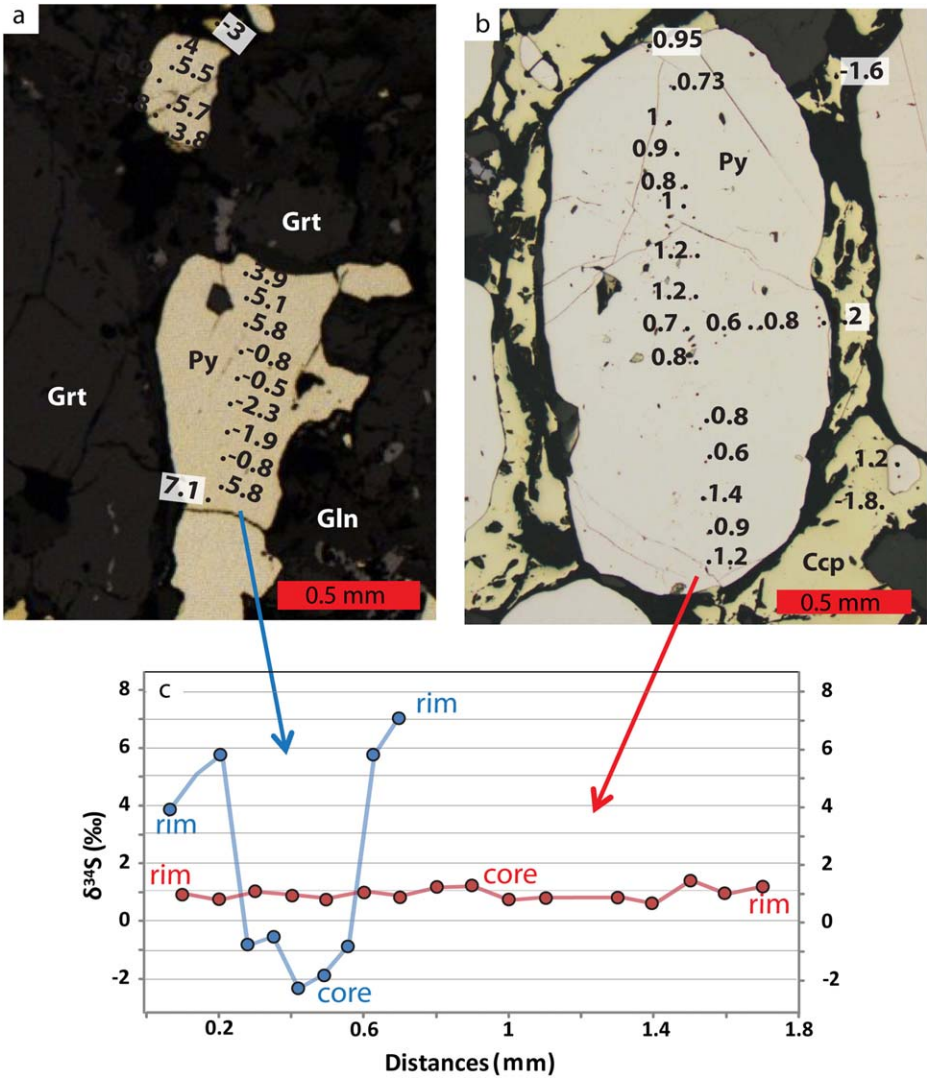

Figure 11. Comparison between isotopically zoned pyrite from the host rock and unzoned pyrite from the massive mineralization. (a) Heterogeneous δ^{34}S values in core-rim zoned pyrite from the matrix of SER18gl. (b) Homogeneous δ^{34}S values from a rounded pyrite in the matrix of sample SER18m. (c) δ^{34}S values measured along transects are reported in a diagram. Ccp = chalcopyrite; Gln = glaucophane; Grt = garnet; Py = pyrite.

Previous workers have established that effective sulfur diffusion through garnet is unlikely at the temperature of interest, so most of the sulfide inclusions in garnet should have behaved as closed systems after inclusion in garnet, as long as the grains are not close to later veins [e.g., *Crowe*, 1994; *Kawakami et al*., 2006]. Therefore, sulfides in garnet should preserve the isotopic composition acquired before garnet crystallization (during pre-Alpine oceanic or during the early stages of prograde metamorphism). Sulfides in the matrix coexist with HP minerals and are likely to record isotopic compositions reflecting peak metamorphism, and/or, possibly, local interaction with retrogression-related fluids.

The limited length-scale isotopic equilibrium recorded by pyrite and disequilibrium recorded by pyrite-chalcopyrite pairs at Servette can be related to partial reequilibration during subduction-related metamorphism. The isotopic heterogeneities in pyrite recognized in every sample (Figures 8, 10, 12a, and 12b), and replacement textures revealed by the irregular distribution of Co in pyrite (Figure 7c) suggest interaction between sulfides and fluids during deformation and recrystallization associated with subduction-related metamorphism. The preservation of this sulfur isotope heterogeneity at the microscale indicates that, at

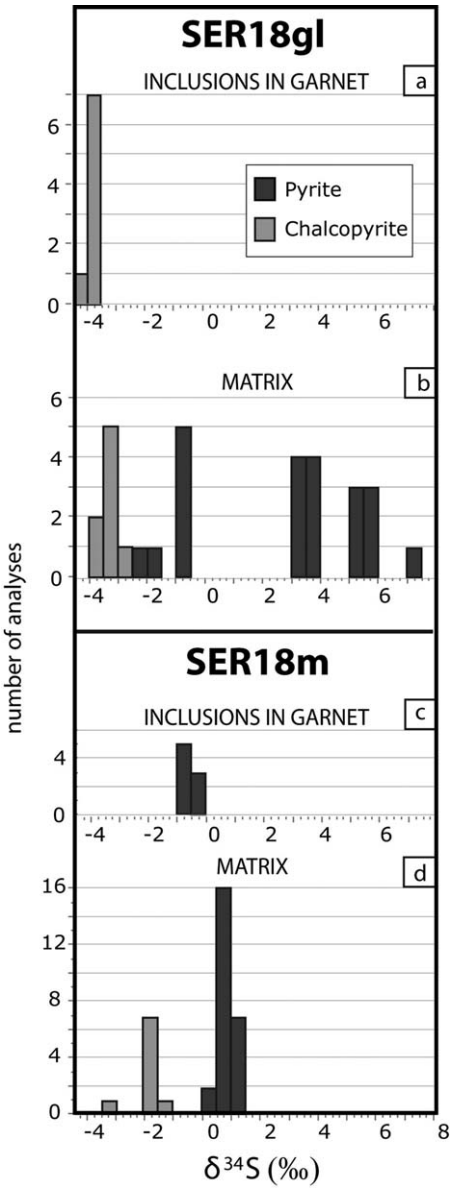

Figure 12. Histograms showing the statistic distribution of δ^{34}S values observed in the host rock (glaucophanite) and in the massive mineralization. Note the different scales of the histograms for appropriate comparison. Light gray is chalcopyrite (ccp) and dark gray is pyrite (py). (a) Sample SER18gl; chalcopyrite in garnet is isotopically similar to that in the matrix (compare with Figure 12b). (b) Sample SER18gl; isotopically heterogeneous pyrite in the matrix. (c) Sample SER18m; pyrite in garnet. (d) Sample SER18m; pyrite and chalcopyrite in the matrix. Note the isotopic homogeneity of pyrite in sample SER18m, compared to other samples.

larger scales, diffusive homogenization of S isotope variability in pyrite is minimal, or does not occur at all, at the P-T conditions experienced by these rocks.

7.3.2. Homogeneous Pyrite δ^{34}S in SER18m

Only sample SER18m records homogeneous δ^{34}S in pyrite. A possible cause for this homogeneity is that the protolith was homogeneous with respect to δ^{34}S. However, this hypothesis is considered unlikely because ocean-floor sulfide massive deposits are typically heterogeneous at the microscale, as observed at Beth-Ghinivert [e.g., *Sangster*, 1971; *Janecky and Seyfried*, 1984; *Alt and Chaussidon*, 1989; *Cook and Hoefs*, 1997; *Velasco et al*., 1998; *Garuti et al*., 2009; *Alt et al*., 2012]. It is therefore more likely that isotopic reequilibration occurred during metamorphism. Isotopic reequilibration may have been facilitated by the high modal abundance of sulfides and by the absence of a silicate matrix [cf. *Crowe*, 1994]. Alternatively, or additionally, minor dissolution and recrystallization in the pyrite matrix may have provided an effective means to focus metamorphic fluids through the massive mineralization, although the extent to which this may have occurred is not known.

7.3.3. Homogeneous Chalcopyrite

In contrast to the heterogeneous δ^{34}S observed in pyrite, δ^{34}S in chalcopyrite is homogeneous, within error, at the mm to cm scale. This observation can be explained by the dramatically different responses of pyrite and chalcopyrite to deformation during metamorphism. Pyrite is brittle during deformation in many natural settings to temperatures well beyond 400°C [*Barrie et al*., 2011], whereas chalcopyrite dynamically recrystallizes at temperatures as low as 300°C [*Cox*, 1987], depending on the differential stress regime and strain rate. Pyrite is consequently sluggish to reequilibrate and tends to preserve original textural and isotopic features more faithfully than chalcopyrite [*Bachinski*, 1977].

Under certain circumstances, this difference in behavior may have contributed to the observed chalcopyrite δ^{34}S values that are too light to have been in equilibrium with coexisting pyrite. If chalcopyrite modes decreased during recrystallization with a loss of heavy sulfur, if chalcopyrite recrystallized in equilibrium with a light sulfur source, or if chalcopyrite modes increased by incorporation of light sulfur then δ^{34}S of chalcopyrite would decrease, without a corresponding decrease in the pyrite δ^{34}S. The occurrence of high $\Delta_{av.py\text{-}ccp}$ values at Beth, as well as Servette, suggests that the process that caused the decoupling of the pyrite and chalcopyrite isotopes was not part of the subduction process. High $\Delta_{av.py\text{-}ccp}$ values could reflect disequilibrium inherited from the protolith, although they could have been produced during retrogression associated with exhumation.

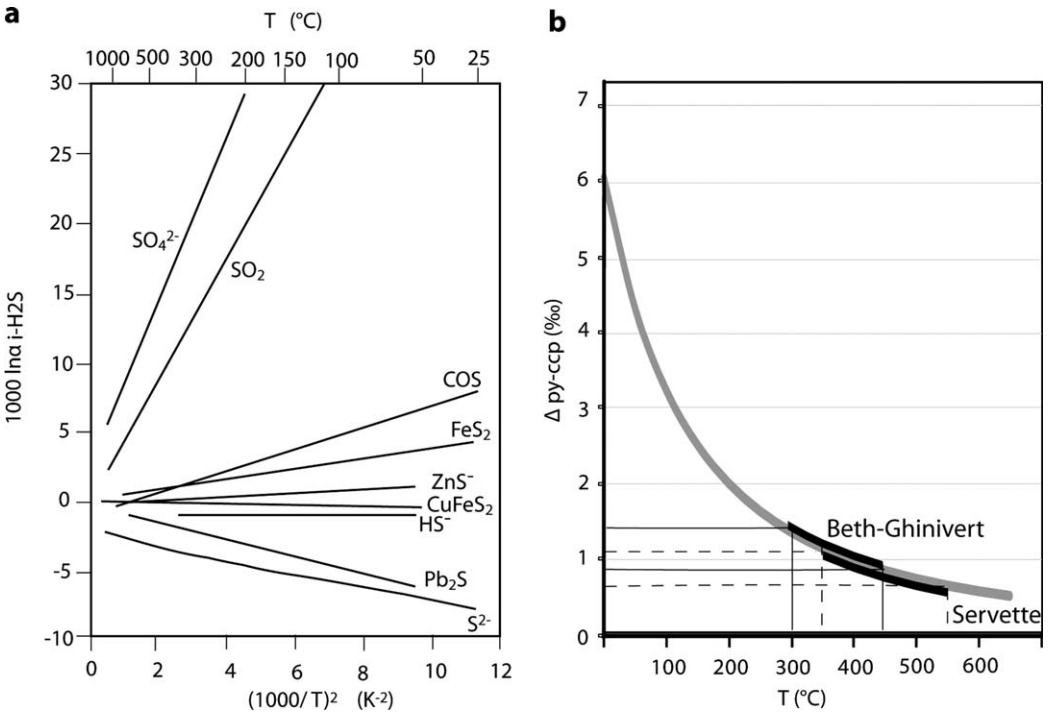

Figure 13. (a) The $1000\ln\alpha_{i\text{-}H2S}$ expresses the fractionation factor between S species "i" and H_2S coexisting at isotopic equilibrium as a function of temperature [after *Seal*, 2006]. (b) $\Delta_{py\text{-}ccp}$ expresses the theoretical difference between $\delta^{34}S$ in pyrite and chalcopyrite at equilibrium as a function of temperature. The black thick lines correspond to the temperature conditions estimated at Servette and Beth-Ghinivert. The dotted lines indicate the theoretical $\Delta_{py\text{-}ccp}$ corresponding values, which are significantly lower than those observed in the studied samples.

7.4. Effects of Pressure, Temperature, Redox, and pH on $\delta^{34}S$

7.4.1. Temperature

Isotopic reequilibration, diffusion rates, and fractionation factors during metamorphism are sensitive to temperature [e.g., *Bachinski*, 1969; *Ohmoto and Rye*, 1979; *Ohmoto and Lasaga*, 1982; *Seal*, 2006]. If sulfur in fluids was dominated by reduced species such as H_2S and HS^- (see below) with a constant isotopic composition during Alpine metamorphism, then evolution of temperatures between 300 and 600°C during prograde and retrograde metamorphism [cf. *Hunziker*, 1974; *Barnicoat and Cartwright*, 1995; *Martin et al.*, 2008] would cause less than 2‰ variation in the $\delta^{34}S$ of pyrite precipitated from a fluid of fixed composition (Figure 13a). Calculations are based on fractionation factors reported by *Seal* [2006]. Thus, temperature variation alone cannot explain the 9.4‰ core-to-rim increase in $\delta^{34}S$ observed in pyrite in sample SER18gl (Figure 11a), or the 14‰ garnet-to-matrix increase in sample SE8 (Figures 10a and 10b).

7.4.2. Pressure

Little is known about the influence of pressure on isotope fractionation, but *Reed and Palandri* [2006] and *Wagner and Boyce* [2006] observed that the solubility of pyrite is minimally affected by pressure compared to temperature. Effects of pressure on S speciation and on isotope fractionation were proposed during degassing of magmas [e.g., *de Moor et al.*, 2011] but these processes can be discounted at Servette, where magmas were not formed. We therefore consider that variations in pressure recorded by the samples studied here did not influence S isotope fractionation directly.

7.4.3. pH

There is no general consensus with respect to the effects of pH on S isotope-fractionation during sulfide-fluid interaction. However, *Wagner and Boyce* [2006] indicated that fractionation between different S-bearing aqueous species is essentially controlled by their oxidation state, with limited influence from pH, so pH effects are discounted here.

7.4.4. Redox and Sulfur Speciation

Calculations reported for analogous metallic parageneses suggest that, at peak metamorphic conditions, fO_2 was $<10^{-20}$ bar and fS_2 was $<10^{-4}$ bar [e.g., *Condie*, 1967; *Itaya et al.*, 1985; *Shi*, 1992; *Kontny et al.*, 1997;

Wood, 1998; *Pokrovski and Dubrovinsky*, 2011, and references therein]. These values are an estimate, at least for Servette, because the original calculations were made at pressures $\leq$1.1 GPa. Extrapolation is necessary because there are no data available for pressures higher than 1.1 GPa.

Pokrovski and Dubrovinsky [2011] proposed that the dominant sulfur species at pressure and temperature above 0.5 GPa and 250°C is the trisulfide ion S^{3-}, but, due to the limited information currently available in the literature about this ion, estimates of its solubility and of isotopic fractionation between this and other sulfur species cannot be performed.

If S^{3-} is excluded from consideration then the dominant sulfur species in solution at the conditions of interest are expected to be H_2S and HS^-, as previously proposed by *Reed and Palandri* [2006], *Wagner and Boyce* [2006], and *Evans et al.* [2014]. Sulfur isotope fractionation between these reduced species is minimal at the temperatures and pressures of interest [*Evans et al.*, 2014], so sulfides crystallized from a fluid would be expected to record the sulfur isotope characteristics of that fluid. Similarly, dissolution of sulfides would not be expected to significantly affect the sulfur isotope composition of the residue.

If sulfate or SO_2-bearing fluids were present then open system processes could have a much stronger effect on sulfur isotope values. ^{34}S sequesters preferentially into more oxidized sulfur species, so a heavy $\delta^{34}S$ value in pyrite could result from formation from, or equilibration with, sulfate-bearing fluids, for example, or a light $\delta^{34}S$ value could result from loss of sulfate derived from pyrite dissolution. However, there is little evidence that conditions were sufficiently oxidizing for sulfate stability during prograde and peak metamorphism.

The occurrence of magnetite only in late greenschist-facies veins may record a decrease of S_2 activity and/or an increase of O_2 activity in retrograde fluids, or it may record the release of ferric iron from prograde minerals such as garnet. If more oxidized fluids were present, then oxidized sulfur species may have coexisted with sulfide phases, with consequences for the sulfur isotope composition of these phases. In this work, we have focused on sulfides Further work is necessary to explore this possibility.

7.5. Conceptual Model

The observed limited metamorphic modification of preexisting S isotope heterogeneities is to be expected if the solubility of S in the metamorphic fluids is low, or if fluids are only sparingly present. In either case, S would be mobilized on very limited length scales, and $\delta^{34}S$ values would be controlled by the isotopic composition of the protoliths on these length scales and by fluid:crystal fractionation factors. Thus, the heterogeneities inherited from the protolith may not be strongly modified by the recrystallization process if sulfur isotope equilibration is limited to length scales of 10–100 s of microns. It therefore seems likely that fluid communication was limited at the sample and, as a consequence, at the deposit scale. Pervasive circulation of S-buffered fluids through hydrothermal ore deposits during shallow-level subduction is therefore not supported by the evidence.

Fluid flow at Beth-Ghinivert is likely to have been more restricted than at Servette, given the preservation of primary isotopic features and the limited evidence for fluid release in neighboring areas within the *Schistes Lustrés* Unit [*Agard et al.*, 2000]. This is consistent with the lower metamorphic P-T conditions at this location and with the estimated structural positions of the deposit in the subducting slab during peak metamorphism (Figure 14); at the depths of $\sim$30 km a large amount of water is retained by sediments and by the oceanic crust, as previously observed in other structurally and genetically comparable areas of the Western Alps [*Phillipot and Scambelluri*, 1996; *Agard et al.*, 2000]. Therefore it is likely that very limited fluid circulation occurred during peak metamorphism Beth-Ghinivert. More intense circulation of metamorphic fluid occurred at Servette, where higher temperatures were attained during subduction, which is consistent with its inferred structural position in the subducting slab (Figure 14).

7.6. Comparison With Previous Works

A number of other studies have produced results consistent with those presented here and attributed the preservation of $\delta^{34}S$ values inherited from the protoliths to limited water release during metamorphic recrystallization [*Alirezaei and Cameron*, 2001; *Hattori and Guillot*, 2007; *Alt et al.*, 2012]. However, there is some evidence for more extensive fluid-induced modification of sulfur isotopes during subduction and exhumation. *Alt et al.* [2013] attributed the modification of the isotopic composition of sulfides in HP serpentinites from the Betic Cordillera to the release of a significant amount of water. *Evans et al.* [2014] used

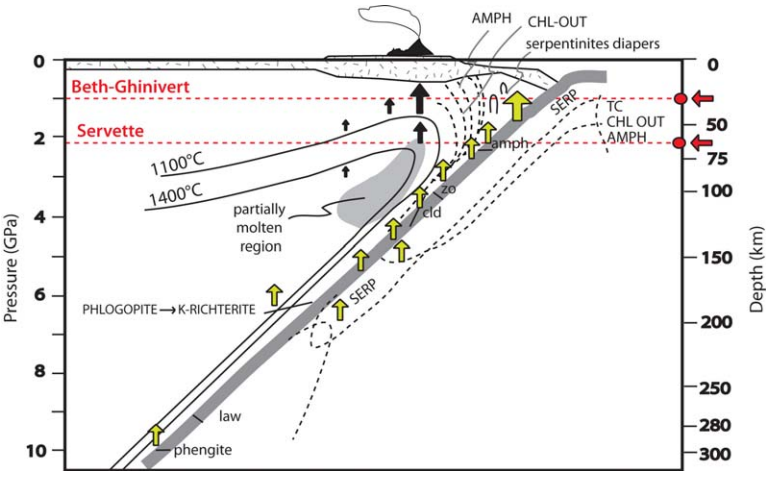

Figure 14. Model for a subduction zones and the formation of a volcanic front [after *Schmidt and Poli*, 1998]. The model highlights the continuous water release up to ~200 km (see green arrows). Dotted red lines indicate pressures and depths estimated for the metamorphic peaks at Beth-Ghinivert [*Giacometti and Rebay*, 2013] and Servette [*Martin et al*., 2008] and help distinguish the position of the two deposits in the subducting slab during the eo-Alpine event.

the results of in situ sulfur isotope analysis to infer that contributions from blueschist-retrogression fluids are recorded by metabasites from the Zermatt Saas, but isotopic heterogeneities preserved at the millimeter scale suggest that fluid/rock ratios were not large enough to be compatible with a fluid-buffered system with respect to sulfur.

It is therefore clear that the extent of sulfur isotope modification varies. Likely causes for the variation include the extent to which fluids were focused through the sampled rocks during metamorphism or retrogression, the extent of deformation, and the pressure and temperature conditions. In situ sampling approaches are more likely to recognize limited length-scale equilibration, whereas bulk sampling approaches provide a useful dm-scale average compositions.

7.7. Implications for Cycling of Sulfur and Chalcophile Elements in Subduction Zones

Despite the evidence of local interaction of sulfides with S-bearing fluids during the different stages of the metamorphic evolution at Servette, the absence of pyrrhotite and magnetite replacing pyrite (through reactions like $FeS_2 = FeS_x + (2 - x)S$) suggests limited S release from the deposit itself. This conclusion is consistent with observations by *Dale et al*. [2009] who studied samples from the Zermatt-Saas Zone and asserted that no significant decrease of S content accompanied recrystallization. Under these circumstances, little or no S would be released from sulfides into the mantle wedge at temperatures lower than, or equal to, those studied.

If breakdown of pyrite and chalcopyrite, which host siderophile and chalcophile elements, in the studied deposits, is limited, then it is unlikely that these elements are mobilized from subducted sulfide ore deposits at pressures and temperatures below that of the blueschist-ecologite transition [cf. *Tomkins*, 2010].

8. Conclusions

Interpretation of S isotopes records in two sulfide deposits from the Italian Western Alps, combined with mineralogical, textural, and geochemical study has provided valuable insights into the mobilization of sulfur and metal-sulfur complexes during the Alpine Orogeny. Evidence of fluid-rock interaction during metamorphism is found at Servette, but not at the lower grade Beth Ghinivert deposit. The low fluid/rock ratio during metamorphism at Beth-Ghinivert is consistent with the depth reached during subduction. Sulfur isotopes were not homogenized at the sample scale within pyrite at either deposit, whereas dynamic recrystallization of chalcopyrite during deformation may have promoted homogenization of S isotopes at short length scales for this mineral.

Neither of the deposits record evidence of intense fluid circulation or sulfide release during metamorphism. Therefore, the release of reduced sulfur to the mantle wedge from subducted sulfide deposits is expected to be minimal at pressure and temperatures less than those of the eclogite facies.

Acknowledgments
The authors acknowledge the facilities and the scientific and technical assistance of the Australian Microscopy and Microanalysis Research Facility at the Centre for Microscopy, Characterization and Analysis, the University of Western Australia, a facility funded by the University, State and Commonwealth Governments. K.E. thanks the Australian Research Council for grant FT120100579 that contributed toward this research. This is a TiGeR paper and a contribution from the ARC Centre of Excellence for Core to Crust Fluid Systems (http://www.ccfs.mq.edu.au). F.G. acknowledges funding from the Italian Ministry of Education, University and Research for his PhD scholarship. J. C. Alt and J. H. Dilles are thanked for carefully reviewing this manuscript. Details of the analyses of S isotopes (δ^{34}S and σ values) which support this work are available as supporting information.

References

Agard, P., B. Goffé, J. L. R. Touret, and O. Vidal (2000), Retrograde mineral and fluid evolution in high-pressure metapelites (Schistes Lustrés unit, Western Alps), *Contrib. Mineral. Petrol.*, *140*, 269–315, doi:10.1007/s004100000190.

Agard, P., L. Jolivet, and B. Goffé (2001), Tectonometamorphic evolution of the Schistes Lustres complex: Implications for the exhumation of HP and UHP rocks in the Western Alps, *Bull. Soc. Geol. Fr.*, *172*(5), 617–636, doi:10.2113/172.5.617.

Alirezaei, S., and E. M. Cameron (2001), Variations of sulfur isotopes in metamorphic rocks from Bamble Sector, southern Norway: A laser probe study, *Chem. Geol.*, *181*, 23–45, doi:10.1016/S0009-2541(01)00266-2.

Alt, J. C., and M. Chaussidon (1989), Ion microprobe analyses of the sulfur isotopic composition of sulfides in hydrothermally altered rocks, DSDP/ODP Hole 504B, *Proc. Ocean Drill. Program Sci. Results*, *111*, 41–45, doi:10.2973/odp.proc.sr.111.151.1989.

Alt, J. C., W. C. Shaks III, and M. C. Jackson (1993), Cycling of sulfur in subduction zones: The geochemistry of sulfur in the Mariana Island Arc and back-arc trough, *Earth Planet. Sci. Lett.*, *119*, 477–494, doi:10.1016/0012-821X(93)90057-G.

Alt, J. C., W. C. Shanks III, L. Crispin, L. Gaggero, E. M. Schwarzenbach, L. Gretchen, G. L. Früh-Green, and S. M. Bernasconi (2012), Uptake of carbon and sulfur during seafloor serpentinization and the effects of subduction metamorphism in Ligurian peridotites, *Chem. Geol.*, *322–323*, 268–277, doi:10.1016/j.chemgeo.2012.07.009.

Alt, J. C., E. M. Schwarzenbach, G. L. Früh-Green, W. C. Shanks III, S. M. Bernasconi, C. J. Garrido, L. Crispini, L. Gaggero, J. A. Padrón-Navarta, and C. Marchesi (2013), The role of serpentinites in cycling of carbon and sulfur: Seafloor serpentinization and subduction metamorphism, *Lithos*, *178*, 40–54, doi:10.1016/j.lithos.2012.12.006.

Angiboust, S., P. Agard, L. Jolivet, and O. Beyssac (2009), The Zermatt-Saas ophiolite: The largest (60 km wide) and deepest (c. 70–80 km) continuous slice of oceanic lithosphere detached from subduction zone?, *Terra Nova*, *21*, 171–180, doi:10.1111/j.1365-3121.2009.00870.x.

Bachinski, D. J. (1977), Sulfur isotopic composition of ophiolitic cupriferous iron sulfide deposits, Notre Dame Bay, Newfoundland, *Econ. Geol.*, *72*, 243–257, doi:10.2113/gsecongeo.72.2.243.

Barnicoat, A. C., and I. Cartwright (1995), Focused fluid flow during subduction: Oxygen isotope data from high-pressure ophiolites of the western Alps, *Earth Planet. Sci. Lett.*, *132*, 53–61, doi:10.1016/0012-821X(95)00040-J.

Barrie, C. D., M. A. Pearce, and A. P. Boyle (2011), Reconstructing the pyrite deformation mechanism map, *Ore Geol. Rev.*, *39*, 265–276, doi:10.1016/j.oregeorev.2011.03.006.

Bebout, G. E. (2007), Metamorphic chemical geodynamics of subduction zones, *Earth Planet. Sci. Lett.*, *260*, 373–393, doi:10.1016/j.epsl.2007.05.050.

Bouquet, J., and M. C. Forette (1973), Sur la deerite de l'ensemble des calchschistes piémontais à Troncea (Italie), *Bull. Soc. Fr. Mineral. Cristallogr.*, *96*, 314–316.

Calvert, S. E., H. G. Thode, D. Yeung, and R. E. Karlin (1996), A stable isotope study of pyrite formation in the Late Pleistocene and Holocene sediments of the Black Sea, *Geochim. Cosmochim. Acta*, *60*(7), 1261–1270, doi:10.1016/0016-7037(96)00020-8.

Carminati, E., and C. Doglioni (2012), Alps vs. Apennines: The paradigm of a tectonically asymmetric Earth, *Earth Sci. Rev.*, *112*, 67–98, doi:10.1016/j.earscirev.2012.02.004.

Cartwright, I., and A. C. Barnicoat (1999), Stable isotope geochemistry of Alpine ophiolites: A window to ocean-floor hydrothermal alteration and constraints on fluid-rock interaction during high-pressure metamorphism, *Int. J. Earth Sci.*, *88*, 219–235, doi:10.1007/s005310050261.

Castellarin, A. (2001), Alps–Apennines and Po Plain-frontal Apennines relations, in *Anatomy of an Orogen: The Apennines and the Adjacent Mediterranean Basins*, edited by G. B. Vai and J. P. Martini, pp. 177–195, Kluwer Acad., Norwell, Mass.

Castello, P. (1981), Inventario delle mineralizzazioni a magnetite, ferro-rame e manganese del complesso piemontese dei calcescisti con pietre verdi in valle d'Aosta, *Ofioliti*, *6*, 5–46.

Chaussidon, M., F. Albarède, and S. M. F. Sheppard (1987), Sulphur isotope heterogeneity in the mantle from ion probe measurements of sulphide inclusions in diamonds, *Nature*, *330*, 242–244.

Condie, K. C. (1967), Oxygen, carbon dioxide and sulfur fugacities during diagenesis and low-grade metamorphism of late precambrian subgraywackes from Northern Utah, *Am. Mineral.*, *52*, 1153–1159.

Cook, N. J., and J. Hoefs (1997), Sulphur isotope characteristics of metamorphosed Cu-(Zn) volcanogenic massive sulphide deposits in the Norwegian Caledonides, *Chem. Geol.*, *135*, 307–324, doi:10.1016/S0009-2541(96)00119-2.

Cooke, D. R. C., and P. H. Hollings (2005), Giant porphyry deposits: Characteristics, distribution, and tectonic controls, *Econ. Geol.*, *100*, 801–818, doi:10.2113/gsecongeo.100.5.801.

Cox, S. F. (1987), Flow mechanisms in sulphide minerals, *Ore Geol. Rev.*, *2*, 133–171, doi:10.1016/0169-1368(87)90026-6.

Crowe, D. E. (1994), Preservation of original hydrothermal δ^{34}S values in greenschist to upper amphibolite volcanogenic massive sulfide deposits, *Geology*, *22*, 873–876, doi:10.1130/0091-7613(1994)022<0873:POOHSV>2.3.CO;2.

Dal Piaz, G. V., J. C. Hunziker and G. Martinotti (1972), La zona Sesia-Lanzo e l'evoluzione tettono-metamorfica delle Alpi nord occidentali interne, *Mem. Soc. Geol. Ital.*, *11*, 433–466.

Dal Piaz, G. V., A. Bistacchi, and M. Massironi (2003), Geological outline of the Alps, *Episodes*, *26*(3), 175–180.

Dale, C. W., K. W. Burton, D. G. Pearson, A. Gannoun, O. Alard, T. W. Argles, and I. J. Parkinson (2009), Highly siderophile element behaviour accompanying subduction of oceanic crust: Whole rock and mineral-scale insights from a high-pressure terrain, *Geochim. Cosmochim. Acta*, *73*, 1394–1416, doi:10.1016/j.gca.2008.11.036.

de Hoog, J. C. M., B. E. Taylor, and M. J. Bergen (2001), Sulfur isotope systematics of basaltic lavas from Indonesia: Implications for the sulfur cycle in subduction zones, *Earth Planet. Sci. Lett.*, *189*, 237–252.

de Moor, J. M., P. L. King, Z. D. Sharp, and T. P. Fischer (2011), A model for sulfur speciation and sulfur isotope fractionation during magmatic degassing on Earth and Mars, paper presented at 42nd Lunar and Planetary Science Conference, Lunar and Planetary Institute, Houston, Texas.

Evans, K. A. (2006), Redox decoupling and redox budgets: Conceptual tools for the study of earth systems, *Geology*, *34*, 489–492, doi:10.1130/G22390.1.

Evans, K. A. (2012), The redox budget of subduction zones, *Earth Sci. Rev.*, *113*, 11–32, doi:10.1016/j.earscirev.2012.03.003.

Evans, K. A., and A. G. Tomkins (2011), The relationship between subduction zone redox budget and arc magma fertility, *Earth Planet. Sci. Lett.*, *308*, 401–409, doi:10.1016/j.epsl.2011.06.009.

Evans, K. A., A. G. Tomkins, J. Cliff, and M. L. Fiorentini (2014), Insights into subduction zone sulfur recycling from isotopic analysis of eclogite-hosted sulfides, *Chem. Geol.*, *365*, 1–19, doi:10.1016/j.chemgeo.2013.11.026.

Garuti, G., A. Pura, J. A. Proenza, and F. Zaccarini (2009), Sulfur-isotope variations in sulfide minerals from massive sulfide deposits of the Northern Apennine Ophiolites: Inorganic and biogenic constrains, *Ofioliti*, *34*(1), 43–62, doi:10.4454/ofioliti.v34i1.377.

Giacometti, F., and G. Rebay (2013), Structural and petrological evolution of the Beth-Ghinivert zone (*Schistes Lustrés*—Italian Western Alps), *Rend. Online Soc. Geol. Ital.*, *29*, 70–73.
Hannington, M. D. (2013), The role of black smokers in the Cu mass balance of the oceanic crust, *Earth Planet. Sci. Lett.*, *374*, 215–226, doi:10.1016/j.espl.2013.06.004.
Hattori, K. H., and S. Guillot (2007), Geochemical character of serpentinites associated with high to ultrahigh-pressure metamorphic rocks in the Alps, Cuba, and the Himalayas: Recycling of elements in subduction zones, *Geochem. Geophys. Geosyst.*, *8*, Q09010, doi:10.1029/2007GC001594.
Hoffman, A. W. (1998), Chemical differentiation of the Earth: The relationship between mantle, continental crust, and oceanic crust, *Earth Planet. Sci. Lett.*, *90*, 297–314, doi:10.1016/0012-821X(88)90132-X.
Hunziker, J. C. (1974), *Rb-Sr and K-Ar Age Determination and the Alpin Tectonic History of The Western Alps*, Mem. degli Ist. di Geol. Mineral. dell'Univ. di Padova., vol. 31, edited by Padova, pp. 1–55.
Itaya, T., R. N. Brothers, and P. M. Black (1985), Sulfides, oxides and sphene in high-pressure schists from new Caledonia, *Contrib. Mineral. Petrol.*, *91*, 151–162, doi:10.1007/BF00377762.
Janecky, D. R., and W. R. Seyfried Jr. (1984), Formation of massive sulfide deposits on ocean ridge crests: Models for mixing between hydrothermal solutions and seawater, *Geochim. Cosmochim. Acta*, *48*, 2723–2738, doi:10.1016/0016-7037(84)90319-3.
Kawakami, T., D. J. Ellis, and A. G. Christy (2006), Sulfide evolution in high-temperature to ultrahigh-temperature metamorphic rocks from Lützow–Holm Complex, East Antarctica, *Lithos*, *92*, 431–446, doi:10.1016/j.lithos.2006.03.057.
Kelley, K. A., and E. Cottrell (2009), Water and the oxidation state of subduction zone magmas, *Science*, *325*, 605–607, doi:10.1126/science.1174156.
Kerrick, D. M., and J. A. D. Connolly (2001), Metamorphic devolatilization of subducted oceanic metabasalts: Implications for seismicity, arc magmatism and volatile recycling, *Earth Planet. Sci. Lett.*, *189*, 19–29, doi:10.1016/S0012-821X(01)00347-8.
Kontny, A., G. Friedrich, H. J. Behr, H. de Wall, E. E. Horn, P. Moller, and G. Zulauf (1997), Formation of ore minerals in metamorphic rocks of the German continental deep drilling site (KTB), *J. Phys. Res.*, *102*(8), 18323–18336, doi:10.1029/96JB03395.
Krutow-Mozgawa, A. (1988), Métamorphisme dans les sédiments riches en fer ou magnesium de la couverture des ophiolites piémontaises (mine de Servette, Val d'Aoste), PhD thesis, 166 pp., Univ. Pierre Marie Curie, Paris.
Lemoine, M., and P. Tricart (1986), Les Schistes lustrés piemontais des Alpes occidentales: Approche stratigraphique, structurale et sédimentologique, *Eclogae Geol. Helv.*, *79*, 271–294.
Lemoine, M., et al. (1986), The continental margin of the Mesozoic Tethys in the Western Alps, *Mar. Pet. Geol.*, *3*, 179–199, doi:10.1016/0264-8172(86)90044-9.
Lemoine, M., P. Tricart, and G. Boillot (1987), Ultramafic and gabbroic ocean floor of the Ligurian Tethys (Alps, Corsica, Apennines): In search of a genetic model, *Geology*, *15*(7), 622–625, doi:10.1130/0091-7613(1987)15<622:UAGOFO>2.0.CO;2.
Manning, C. E. (2004), The chemistry of subduction-zone fluids, *Earth Planet. Sci. Lett.*, *223*, 1–16, doi:10.1016/j.epsl.2004.04.030.
Manning, C. E. (2011), Sulfur surprises in deep geological fluids, *Science*, *331*, 1018–1019, doi:10.1126/science.1202468.
Marini, L., R. Moretti, and M. Accornero (2011), Sulfur isotopes in magmatic-hydrothermal systems, melts and magmas, *Rev. Mineral. Geochem.*, *73*, 423–492, doi:10.2138/rmg.2011.73.14.
Marshall, B., and L. B. Gillian (1993), Remobilization, syn-tectonic processes and massive sulfide deposits, *Ore Geol. Rev.*, *8*, 39–64, doi:10.1016/0169-1368(93)90027-V.
Martin, S., G. Godard, and G. Rebay (2004), Walking on a Palaeo Ocean floor. The subducted tethys in the Western Alps—An excursion guide, *J. Virtual Explorer*, *16*(2), 1–46.
Martin, S., G. Rebay, J. R. Kienast, and C. Mével (2008), An eclogitised oceanic paleo-hydrothermal field from the St. Marcel Valley (Italian Western Alps), *Ofioliti*, *33*(1), 49–63, doi:10.4454/ofioliti.v33i1.359.
Natale, P. (1966), Sulla pirite di alcuni giacimenti piritoso-cupriferi stratiformi delle Alpi Occidentali, *Bollettino della Associazione Mineraria Subalpina*, *3–4*, 356–363.
Natale, P. (1969), Re-crystallization and remobilization in some stratiform pyrite deposits of the Western Alps, paper presented at Convegno Sulla Rimobilizzazione dei Minerali Metallici e Non Metallici, Università degli Studi di Cagliari, Cagliari, Italy.
Natale, P., and A. Visetti (1980), Contributo alla conoscenza minerogenica delle piriti di origine esalativo-sedimentaria, *Bollettino della Associazione Mineraria Subalpina*, *1*, 180–210.
Natale, P., and S. Zucchetti (1966), Studi sui giacimenti piritoso-cupriferi stratiformi della Alpi Occidentali—Nota I. Compendio selle conoscenze attuali delle piriti stratiformi, *L'Industria Mineraria*, *17*, 443–451.
Novarese, V. (1900), La miniera del Beth e Ghinivert. Rassegna mineraria della industria chimica e delle industrie mineralurgiche e metallurgiche, 12, 7 (97–99), 8 (113–115), and 9 (131–133).
Ohmoto, H., and M. B. Goldhaber (1997), Sulfur and carbon isotopes, in *Geochemistry of Hydrothermal Ore Deposits*, edited by H. L. Barnes, pp. 517–611, John Wiley, N. Y.
Ohmoto, H., and A. C. Lasaga (1982), Kinetics of reactions between aqueous sulfates and sulfides in hydrothermal systems, *Geochim. Cosmochim. Acta*, *46*, 1727–1745, doi:10.1016/0016-7037(82)90113-2.
Ohmoto, H., and R. O. Rye (1979), Isotopes of sulfur and carbon, in *Geochemistry of Hydrothermal Ore Deposits*, edited by H. L. Barnes, pp. 509–567, John Wiley, N. Y.
Phillipot, P., and M. Scambelluri (1996), The composition and behaviour of fluids in high-pressure rocks from the Alps: A review, in *Studies on Metamorphic Rocks and Minerals of the Western Alps. A Volume in Memory of Ugo Pognante, Boll. Museo Reg. Sci. Nat.*, vol. 13, edited by B. Lombardo, pp. 75–102, Torino, Italy.
Plank, T., and C. H. Langmuir (1998), The chemical composition of subducting sediment and its consequences for the crust and mantle, *Chem. Geol.*, *145*, 325–394, doi:10.1016/S0009-2541(97)00150-2.
Pognante, U. (1991), Petrological constrains on the eclogite- and blueschist-facies metamorphism and P-T-t path in western Alps, *J. Metamorph. Geol.*, *9*, 5–17, doi:10.1111/j.1525-1314.1991.tb00501.x.
Polino, R., G. V. Dal Piaz, and G. Gosso (1990), Tectonic erosion at the Adria Margin and accretionary processes for the Cretaceous orogeny of the Alps, *Mem. Soc. Geol. Fr.*, *156*, 345–367.
Pokrovski, G. S., and L. S. Dubrovinsky (2011), The S^{3-} ion is stable in geological fluids at elevated temperatures and pressures, *Science*, *331*, 1052–1054, doi:10.1126/science.1199911.
Puchelt, H., and H. W. Hubberten (1980), Preliminary results of sulfur isotope investigations on deep sea drilling project cores from Legs 52 and 53, in *Initial Reports of the Deep Sea Drilling Project*, edited by T. Donnelly et al., vol. 51–53, pp. 1145–1148, U.S. Gov. Print. Off., Washington, D. C.
Rebay, G., and R. Powell (2012), Eclogite-facies sea-floor hydrothermally-altered rocks: Calculated phase equilibria for an example from the Western Alps at Servette, *Ofioliti*, *37*(1), 55–63, doi:10.4454/ofioliti.v37i1.405.

Rubatto, D., D. Gebauer, and M. Fanning (1998), Jurassic formation and eocene subduction of the Zermatt-Saas-Fee ophiolites: Implications for the geodynamic evolution of the Central and Western Alps, *Contrib. Mineral. Petrol.*, *132*, 269–287, doi:10.1007/s004100050421.

Reed, M. H., and J. Palandri (2006), Sulfide mineral precipitation from hydrothermal fluids, *Rev. Mineral. Geochem.*, *61*, 609–631, doi:10.2138/rmg.2006.61.11.

Sangster, D. F. (1971), Sulphur isotopes, stratabound sulphide deposits, and ancient seas, Soc. Mining Geol. Japan, Special Issue Proc. IMA-IAGOD Meeting 70-3, 295–299.

Sawkins, F. J. (1990), Integrated tectonic-genetic model for volcanic-hosted massive sulfide deposits, *Geology*, *18*, 1061–1064, doi:10.1130/0091-7613(1990)018<1061:ITGMFV>2.3.CO;2.

Scambelluri, M., G. B. Piccardo, P. Philippot, A. Robbiano, and L. Negretti (1997), High salinity fluid inclusions formed from recycled seawater in deeply subducted alpine serpentinite, *Earth Planet. Sci. Lett.*, *148*, 485–499, doi:10.1016/S0012-821X(97)00043-5.

Scambelluri, M., O. Müntener, L. Ottolini, T. T. Pettke, and R. Vannucci (2004), The fate of B, Cl and Li in the subducted oceanic mantle and in the antigorite breakdown fluids, *Earth Planet. Sci. Lett.*, *222*, 217–234, doi:10.1016/j.epsl.2004.02.012.

Schmidt, M. W., and S. Poli (1998), Experimentally based water budgets for dehydrating slabs and consequences for arc magma generation, *Earth Planet. Sci. Lett.*, *163*, 361–379, doi:10.1016/S0012-821X(98)00142-3.

Schwarzenbach, E. M., G. L. Früh-Green, S. M. Bernasconi, J. C. Alt, W. C. Shanks III, L. Gaggero, and L. Crispini (2012), Sulfur geochemistry of peridotite-hosted hydrothermal systems: Comparing the Ligurian ophiolites with oceanic serpentinites, *Geochim. Cosmochim. Acta*, *91*, 283–305, doi:10.1016/j.gca.2012.05.021.

Seal, R. R. (2006), Sulfur isotope geochemistry of sulfide minerals, *Rev. Mineral. Geochem.*, *61*, 633–677, doi:10.2138/rmg.2006.61.12.

Shi, P. (1992), Fluid fugacities equilibria in the Fe-Si-O-H-S system, *Am. Mineral.*, *77*, 1050–1066.

Sillitoe, H. R. (1972a), A plate tectonic model for the origin of porphyry copper deposits, *Econ. Geol.*, *67*, 184–197, doi:10.2113/gsecongeo.67.2.184.

Sillitoe, H. R. (1972b), Geology of the Los Pelambres porphyry copper deposit, Chile, *Econ. Geol.*, *68*, 1–10, doi:10.2113/gsecongeo.68.1.1.

Spandler, C., and C. Pirard (2013), Element recycling from subducting slabs to arc crust: A review, *Lithos*, *170–171*, 208–223, doi:10.1016/j.lithos.2013.02.016.

Strauss, H., and J. Schieber (1990), A sulfur isotope study of pyrite genesis: The mid-Proterozoic Newland Formation, Belt Supergroup, Montana, *Geochim. Cosmochim. Acta*, *54*(1), 197–204, doi:10.1016/0016-7037(90)90207-2.

Tartarotti, P., S. Martin, and R. Polino (1986), Geological data about the ophiolitic sequences in the St. Marcel Valley (Aosta Valley), *Ofioliti*, *11*(3), 343–346.

Tomkins, A. G. (2007), Three mechanisms of ore remobilisation at the amphibolite facies Montauban Zn-Pb-Au-Ag deposit, *Miner. Deposita*, *42*, 627–637, doi:10.1007/s00126-007-0131-9.

Tomkins, A. G. (2010), Windows of metamorphic sulfur liberation in the crust: Implications for gold deposit genesis, *Geochim. Cosmochim. Acta*, *74*, 3246–3259, doi:10.1016/j.gca.2010.03.003.

Tricart, P., and S. Schwartz (2006), A north-south section across the Queyras Schistes lustrés (Piedmont zone, Western Alps): Syn-collision refolding of a subduction wedge, *Eclogae Geol. Helv.*, *99*, 429–442, doi:10.1007/s00015-006-1197-6.

Velasco, F., J. Sánchez-España, A. J. Boyce, A. E. Fallick, R. Sáez, and G. R. Almodóvar (1998), A new sulphur isotopic study of some Iberian Pyrite Belt deposits: Evidence of a textural control on sulphur isotope composition, *Miner. Deposita*, *24*, 4–18, doi:10.1007/s001260050182.

Wagner, T., and A. J. Boyce (2006), Pyrite metamorphism in the Devonian Hunsrück slate of Germany: Insights from laser microprobe sulfur isotope analysis and thermodynamic modeling, *Am. J. Sci.*, *306*, 525–552, doi:10.2475/07.2006.02.

Wood, S. A. (1998), Calculation of activity-activity and log fO_2—pH diagrams, in *Techniques in Hydrothermal Ore Deposits Geology, Rev. Econ. Geol.*, vol. 10, edited by J. P. Richards and P. B. Larson, Soc. of Econ. Geol. Inc., Littleton, Colo.